

Enhancing Morphological Measurements of Cosmic Web with Delaunay Tessellation Field Estimation

YU LIU ^{1,2,3} YU YU ^{2,3} PENGJIE ZHANG ^{2,3,4} AND HAO-RAN YU ⁵

¹Department of Astronomy, Tsinghua University, Beijing, 100084, P.R. China

²Department of Astronomy, School of Physics and Astronomy, Shanghai Jiao Tong University, Shanghai, 200240, P.R. China

³Key Laboratory for Particle Astrophysics and Cosmology (MOE)/Shanghai Key Laboratory for Particle Physics and Cosmology, P.R. China

⁴Tsung-Dao Lee Institute, Shanghai Jiao Tong University, Shanghai, 200240, P.R. China

⁵Department of Astronomy, Xiamen University, Xiamen, Fujian, 361005, P. R. China

ABSTRACT

The density fields constructed by traditional mass assignment methods are susceptible to irritating discreteness, which hinders morphological measurements of cosmic large-scale structure (LSS) through Minkowski functionals (MFs). For alleviating this issue, fixed-kernel smoothing methods are commonly used in literatures, at the expense of losing substantial structural information. In this work, we propose to measure MFs with Delaunay tessellation field estimation (DTFE) technique, with the goal to maximize extractions of morphological information from sparse tracers. We perform our analyses starting from matter fields and progressively extending to halo fields. At matter field level, we elucidate how discreteness affects the morphological measurements of LSS. Then, by comparing with traditional Gaussian smoothing scheme, we preliminarily showcase the advantages of DTFE for enhancing measurements of MFs from sparse tracers. At halo field level, we first numerically investigate various systematic effects on MFs of DTFE fields, which are induced by finite voxel sizes, halo number densities, halo weightings, and redshift space distortions (RSDs), respectively. Then, we explore the statistical power of MFs measured with DTFE for extracting cosmological information encoded in RSDs. We find that MFs measured with DTFE exhibit improvements by ~ 2 orders of magnitude in discriminative power for RSD effects and by a factor of ~ 3 -5 in constraining power on structure growth rate over the MFs measured with Gaussian smoothing. These findings demonstrate the remarkable enhancements in statistical power of MFs achieved by DTFE, showing enormous application potentials of our method in extracting various key cosmological information from galaxy surveys.

Keywords: methods: data analysis – methods: statistical – cosmology: large-scale structure of Universe

1. INTRODUCTION

Ambitious on-going and up-coming cosmological surveys [e.g., HETDEX (Hill et al. 2008), LSST (LSST Science Collaboration et al. 2009), Euclid (Laureijs et al. 2011), 4MOST (de Jong et al. 2012), PFS (Takada et al. 2014), SPHEREX (Doré et al. 2014), DESI (DESI Collaboration et al. 2016), WFIRST (Doré et al. 2018), and CSST (Gong et al. 2019)], particularly the fifth-generation surveys [e.g., WST (Ellis & Dawson 2019), MSE (Percival et al. 2019), MegaMapper (Schlegel et al. 2019), and MUST¹], will provide high-precision map of cosmic large-scale structure (LSS), which encodes a wealth of valuable cosmological information about our Universe. Efficient extractions of these critical information will help us greatly deepen our understanding of many key fundamental questions in cosmology (e.g., dark energy properties, neutrino masses, gravity and inflation models, etc.). This necessitates the development of powerful statis-

tical tools to characterize or quantify LSS properties from various angles.

Two-point statistics (i.e., two-point correlation function and power spectrum) have played crucial roles in the analyses of LSS data, especially for studies on baryonic acoustic oscillations (e.g., Eisenstein et al. 2005; Alam et al. 2017; Bautista et al. 2021; Moon et al. 2023). These statistics characterize the clustering properties of LSS, but can only give a complete description for Gaussian random field. In reality, LSS has evolved into a highly non-Gaussian field in the present-day Universe, which makes them can not capture appreciable non-Gaussian information on small scales, thus requiring measurements of an infinite hierarchy of N -point statistics (i.e., N -point correlation functions and polyspectra). At present, accurate measuring and theoretical modelling higher-order N -point statistics are challenging², due to the complexities in all possible combinations of multiplets. Moreover, even if the first N -order information is extracted, other interesting information may still remain in higher-order terms.

Corresponding author: Yu Liu; Yu Yu; Pengjie Zhang
liuyu9@tsinghua.edu.cn; yuyu22@sjtu.edu.cn; zhangpj@sjtu.edu.cn

¹ Multiplexed Survey Telescope (MUST): <https://must.astro.tsinghua.edu.cn/must/en/index.html>

² Still, some specific progresses have been made recently in this direction (see Philcox & Slepian 2021; Hou et al. 2021; Philcox et al. 2022 and Refs. therein).

Consequently, various summary statistics for non-Gaussian information have been proposed as potential supplements to two-point statistics, e.g., count in cells (de Lapparent et al. 1991; Uhlemann et al. 2020; Repp & Szapudi 2020), void statistics (Chan et al. 2014; Zhao et al. 2016; Kreisch et al. 2019), peak statistics (Gay et al. 2012; Shan et al. 2014; Liu et al. 2015a; Liu et al. 2015b), Voronoi statistics (Paranjape & Alam 2020; Jamieson & Loverde 2021), and even scattering transform (Cheng et al. 2020; Cheng & Ménard 2021), etc. In particular, morphological statistical methods [e.g., β -Skeleton (Fang et al. 2019; Suárez-Pérez et al. 2021), Betti numbers (Pranav et al. 2017; Pranav et al. 2019; Giri & Mellema 2021), persistent topology (Elbers & van de Weygaert 2019, 2023; Wilding et al. 2021; Jalali Kanafi et al. 2023; Bermejo et al. 2024; Yip et al. 2024), minimal spanning tree (Barrow et al. 1985; Naidoo et al. 2021), cosmic web skeleton (Novikov et al. 2006; Sousbie et al. 2008), wavelet analyses (Martinez et al. 1993; Arnalte-Mur et al. 2012), shape statistics (Sahni et al. 1998; Basilakos 2003), genus statistics (Gott et al. 1986; Hamilton et al. 1986; Appleby et al. 2021), Minkowski tensors (Appleby et al. 2018a; Appleby et al. 2018b), Minkowski functionals (Mecke et al. 1994; Liu et al. 2020; Matsubara et al. 2022), etc.] are actively employed to characterize the geometrical and topological properties of LSS, providing alternative ways to capture higher-order information directly, in complementary to traditional N -point formalism.

As a conceptual generalization of genus (Mecke et al. 1994; Schmalzing & Buchert 1997), Minkowski functionals (MFs) can elegantly describe the global characterizations of morphological properties of LSS, and have been employed in various cosmological studies [e.g., detecting primordial non-Gaussianities (Hikage et al. 2006; Hikage et al. 2008; Planck Collaboration et al. 2016; Ducout et al. 2013), serving as standard ruler (Park & Kim 2010; Zunckel et al. 2011; Blake et al. 2014), constraining cosmological parameters (Appleby et al. 2018c; Appleby et al. 2021; Appleby et al. 2022), probing neutrino masses (Marques et al. 2019; Liu et al. 2020; Liu et al. 2022), analyzing effects of redshift space distortions (Codis et al. 2013; Jiang et al. 2021), testing cosmologies and gravities (Hikage et al. 2003; Wang et al. 2012; Fang et al. 2017), etc.]. One popular method [other method can also be found in literatures, i.e., the germ-grain approach (cf. Mecke et al. 1994; Wiegand et al. 2014)] for measuring MFs is the iso-density approach, which we will focus on in our study (see Section 2). The MFs measured in this way can be well theoretically modelled for Gaussian (Tomita 1990; Schmalzing & Buchert 1997; Matsubara 2003) and weakly non-Gaussian (Matsubara 1994; Matsubara 2003; Pogosyan et al. 2009; Matsubara 2010; Gay et al. 2012; Matsubara & Kuriki 2021; Matsubara et al. 2022) fields [even for the fields with RSDs (Matsubara 1996; Codis et al. 2013)], showing distinct advantages over the germ-grain approach.

The iso-density approach estimates four MFs with a series of excursion sets, which are specified by a series of iso-density contours of LSS. Therefore, this method relies heavily on the reconstruction of underlying continuous density field from discrete point tracers. In realistic applications, the number densities of tracers (i.e., halos/galaxies) are low, thereby in-

ducing significant shot noises (i.e., discreteness effects) in the tracer fields constructed by commonly used mass assignment methods [i.e., Nearest Grid Point (NGP), Cloud-in-Cell (CIC), Triangular-Shaped Cloud (TSC), etc.]. As a result, this renders the tracer fields to be exceedingly discontinuous. To alleviate this problem, smoothing methods with fixed kernel widths, at least larger than the mean tracer spacing, are commonly employed in previous studies. These methods can help eliminate noise components and produce nicely smoothed continuous fields. However, meanwhile, the recipes of fixed smoothing will also erode the texture of underlying density distribution, i.e., discarding substantial structural information below the scales of kernel widths, consequently downgrading the statistical power of MFs in various cosmological studies (cf. Zhang et al. 2010; Jiang et al. 2023).

In this study, we opt for Delaunay Tessellation Field Estimator (DTFE)³ (Schaap & van de Weygaert 2000; van de Weygaert & Schaap 2009; van de Weygaert et al. 2009; Cautun & van de Weygaert 2011a; Cautun & van de Weygaert 2011b) to address this issue⁴. This method can help to recover the largest number of structural elements from point sets, allowing for extracting maximum amount of morphological information with MFs. Therefore, the statistical power of MFs with DTFE (hereafter DTFE MFs) can be significantly enhanced, over the fixed smoothing methods (Zhang et al. 2010). We first demonstrate this at matter field level and further extend it to halo field level. In particular, for DTFE MFs of halo fields, we numerically explore various main systematic effects, caused by finite voxel size, halo number density, halo-weighting scheme, and RSDs, on their measurements, and showcase their strong discriminative and constraining power in RSD studies. Hopefully, the applications of DTFE will dramatically improve the performance of MFs in extracting various key cosmological information (e.g., neutrino masses (Liu et al. 2020), modified gravities (Fang et al. 2017), primordial non-Gaussianities (Hikage et al. 2006; Hikage et al. 2008), and cosmological parameters (Appleby et al. 2020; Appleby et al. 2022), etc.) from sparse tracers.

Historically, due to its exceptional characteristics, DTFE has been applied in various advanced pipelines for characterizing, identifying, and classifying structures of LSS. Examples include MMF (Aragón-Calvo et al. 2007) and NEXUS (Cautun et al. 2013), which leverage multi-scale geometry of structural components, and SpineWeb (Aragón-Calvo et al. 2010) and DisPerSE (Sousbie 2011; Sousbie et al. 2011), which utilize topology of cosmic web via Morse theory (Morse 1934; Milnor 1963; Jost & Jost 2008). Also, DTFE has been employed in WVF (Platen et al. 2007), the first watershed-based void finder that can identify cosmic voids irrespective of sizes and shapes. Subsequently, Neyrinck 2008 proposed a closely related technique, ZOBOV, based on Voronoi Tessellation Field Estimator (VTFE) (cf. Schaap 2007). Thereafter, later watershed-based void find-

³ Delaunay Tessellation Field Estimator (DTFE): <https://github.com/MariusCautun/DTFE>

⁴ Previously, Martínez et al. 2005 attempted to use wavelet-denoising method to alleviate the problem induced by fixed-kernel smoothing. Additionally, Zhang et al. 2010 endeavored to boost topological information of genus statistics with DTFE.

ing pipelines, such as VIDE (Sutter et al. 2015), REVOLVER (Nadathur et al. 2019), and V^2 (Douglass et al. 2022; Douglass et al. 2023), are built upon ZOBOV. In addition, DTFE can construct not only continuous density fields but also volume-covering velocity fields and their corresponding divergences, shears, and vorticities (Bernardeau & van de Weygaert 1996; Romano-Díaz & van de Weygaert 2007; van de Weygaert & Schaap 2009).

This paper is structured as follows. In Section 2, we give a brief overview for MFs. In Section 3, we describe the basic DTFE algorithm for generating continuous fields from point sets. In Section 4, we introduce in detail the data used in this work. In Section 5, we preliminarily demonstrate the advantages of DTFE in measuring MFs from sparse point set, at matter field level. Then, at halo field level, we investigate various main systematic effects on DTFE MFs in Section 6 and show strong statistical power of DTFE MFs in extracting cosmological information in Section 7. Finally, we give summaries and discussions in Section 8. Appendix A shows the details of our strategy to determine the smoothing lengths used in Gaussian smoothing method. Appendix B displays the RSD signals and the associated RSD signal-to-noise (S/N) ratios extracted from DTFE MFs. Appendix C presents the technical details of Fisher forecasts employed in our study.

2. MINKOWSKI FUNCTIONALS

MFs are a family of morphological (i.e., geometrical and topological) descriptors with properties of additivity, motion invariance, and conditional continuity for any manifold in D -dimensional space. These descriptors are originally derived from the theory of convex bodies and integral geometry, and were first introduced into cosmology by Ref. Mecke et al. 1994 to characterize the morphology (i.e., geometry and topology) of cosmic web. According to Hadwiger’s theorem (Hadwiger Springer, Berlin, 1957), the topo-geometrical properties of any given manifold in D -dimensional space can be completely characterized by $D + 1$ MFs. Thus, it opens a unique way to comprehensively access all orders of N -point correlation information at once.

In LSS studies, the manifolds (\mathbb{M}) of typical interests are excursion sets (E_ν) of 3D cosmological scalar fields (i.e., dark matter fields or halo/galaxy fields),

$$E_\nu = \{\mathbf{x} \in \mathbb{M} : \nu(\mathbf{x}) \geq \nu\}, \quad (1)$$

where E_ν is the set of all points \mathbf{x} with density $\nu(\mathbf{x}) \geq \nu$ and ν is the density threshold serving as diagnostic parameter for displaying morphological features. Four MFs quantify the enclosed volume (V_0) of E_ν , as well as the surface’s area (V_1), integrated mean curvature (V_2), and Euler characteristic (V_3) of the set boundary ∂E_ν (i.e., the iso-density surface),

$$\begin{aligned} V_0(\nu) &= \frac{1}{|\mathcal{D}|} \int_{E_\nu} d^3x, \\ V_1(\nu) &= \frac{1}{6|\mathcal{D}|} \int_{\partial E_\nu} dS(\mathbf{x}), \\ V_2(\nu) &= \frac{1}{6\pi|\mathcal{D}|} \int_{\partial E_\nu} \left(\frac{1}{R_1(\mathbf{x})} + \frac{1}{R_2(\mathbf{x})} \right) dS(\mathbf{x}), \\ V_3(\nu) &= \frac{1}{4\pi|\mathcal{D}|} \int_{\partial E_\nu} \frac{1}{R_1(\mathbf{x})R_2(\mathbf{x})} dS(\mathbf{x}), \end{aligned} \quad (2)$$

where $R_1(\mathbf{x})$ and $R_2(\mathbf{x})$ are two principal radii of curvature of the set’s surface orientated toward lower-density regions. These quantifiers provide complete morphological description, including size (i.e., V_0 and V_1), shape (i.e., V_2), and connectivity (i.e., V_3) of the excursion sets. In particular, according to Gauss-Bonnet theorem, the last MF (i.e., Euler characteristic) is simply related to the number of isolated regions (balls), empty regions inside balls (bubbles), and holes in ball surfaces (tunnels) per unit volume,

$$V_3 = \frac{1}{|\mathcal{D}|} (N_{\text{ball}} + N_{\text{bubble}} - N_{\text{tunnel}}), \quad (3)$$

having direct relation with genus ($G = 1 - V_3$), which is the first topological descriptor (e.g., Gott et al. 1986) widely used in cosmic web’s topological analyses.

Two standard grid-based numerical algorithms to compute MFs from regularly gridded density field⁵, i.e., Koenderink invariant from differential geometry (Schneider 1993) and Crofton’s formula from integral geometry (Hadwiger Springer, Berlin, 1957; Mecke 1979), have been developed in literatures (Schmalzing & Buchert 1997). In this work, we employ Crofton’s formula to quote our results, because it is more stable and is the most commonly used method in previous works. All MFs are measured as functions of density threshold $\nu \equiv 1 + \delta$ with $\nu \in [0.003, 1000]$, where δ is the density contrast. The error bars are estimated via the standard errors of MFs, i.e., $s_e = \sigma/\sqrt{n_f}$. Here, σ is the standard deviation of MFs, calculated from n_f subfields obtained by equally subdividing the original field. For DM and halo fields, the numbers of subfields are $n_f = 4^3 = 64$ and $n_f = 8^3 = 512$, respectively. Since the error bars are too tiny to be visible in most scenarios, they are omitted in all figures in this paper, except for Fig. 12 and Fig. 13. Note that all MFs are visualized by logarithmic x-axis, considering that probability distribution function of LSS roughly obeys log-normal form at low redshift.

3. DELAUNAY TESSELLATION FIELD ESTIMATION

Given the positions of a set of points \mathbf{x}_i (generators) with weights w_i ($i = 1, 2, 3 \dots N$) in D -dimensional space, the first step of DTFE procedure is to self-adaptively tessellate the space into a union of space-filling and mutually disjoint Delaunay cells [i.e., simplexes, which are triangles (tetrahedra) in 2D (3D) space] using the Delaunay tessellation technique, which imposes the circumsphere of each tetrahedron does not contain any generators. Under the assumption of uniform sampling (i.e., the point set is an unbiased sample of the underlying density field), the estimated density at each generator \mathbf{x}_i is determined by the normalized inverse of the volume of its contiguous Voronoi cell $V(\mathcal{W}_i)$ (see van de Weygaert & Schaap 2009 for more technical details),

$$\hat{\rho}(\mathbf{x}_i) = (1 + D) \frac{w_i}{V(\mathcal{W}_i)}, \quad (4)$$

⁵ In literatures, several novel triangulation-based algorithms (cf. Sheth et al. 2003; Aragon-Calvo et al. 2010; Lippich & Sánchez 2021), which estimate MFs by using triangulated iso-density surfaces, have also been proposed in succession, aiming to improve the accuracies of MFs’ estimations.

where the contiguous Voronoi cell \mathcal{W}_i is the union of all adjacent Delaunay cells $\mathcal{D}_{\mathbf{x}_i}^{\text{adj}}$ with \mathbf{x}_i as one of their $D + 1$ vertices,

$$V(\mathcal{W}_i) = \sum V(\mathcal{D}_{\mathbf{x}_i}^{\text{adj}}). \quad (5)$$

In real survey data (i.e., galaxy samples), the point set is actually always modulated by specified selection process (i.e., systematic non-uniform sampling), which can be quantified by a priori selection function $\psi(\mathbf{x}_i)$ varying with sky position and redshift. In this scenario, the equation (4) will be generalized to be

$$\widehat{\rho}(\mathbf{x}_i) = (1 + D) \frac{w_i}{\psi(\mathbf{x}_i) V(\mathcal{W}_i)}. \quad (6)$$

To obtain a continuous field, the density values inside a Delaunay cell, at position $\mathbf{x} = (x^1, x^2, x^3 \dots x^D)$, then are estimated by multi-dimensional linear interpolation from the $D + 1$ density values of cell's vertices $\widehat{\rho}(\mathbf{x}_n)$ ($n = 0, 1, 2, 3 \dots D$)⁶,

$$\widehat{\rho}(\mathbf{x}) = \widehat{\rho}(\mathbf{x}_0) + \widehat{\nabla}\rho \cdot (\mathbf{x} - \mathbf{x}_0). \quad (7)$$

Here, $\widehat{\nabla}\rho$ is the linear constant gradient inside the cell, which can be calculated by

$$\widehat{\nabla}\rho = \begin{pmatrix} \frac{\partial \widehat{\rho}}{\partial x^1} \\ \frac{\partial \widehat{\rho}}{\partial x^2} \\ \frac{\partial \widehat{\rho}}{\partial x^3} \\ \vdots \\ \frac{\partial \widehat{\rho}}{\partial x^D} \end{pmatrix}^T = \mathbf{J}^{-1} \begin{pmatrix} \Delta \widehat{\rho}_1 \\ \Delta \widehat{\rho}_2 \\ \Delta \widehat{\rho}_3 \\ \vdots \\ \Delta \widehat{\rho}_D \end{pmatrix}; \quad (8)$$

$$\mathbf{J} = \begin{pmatrix} \Delta x_1^1 & \Delta x_1^2 & \Delta x_1^3 & \dots & \Delta x_1^D \\ \Delta x_2^1 & \Delta x_2^2 & \Delta x_2^3 & \dots & \Delta x_2^D \\ \Delta x_3^1 & \Delta x_3^2 & \Delta x_3^3 & \dots & \Delta x_3^D \\ \vdots & \vdots & \vdots & \ddots & \vdots \\ \Delta x_D^1 & \Delta x_D^2 & \Delta x_D^3 & \dots & \Delta x_D^D \end{pmatrix}, \quad (9)$$

where $\Delta \widehat{\rho}_n = \widehat{\rho}(\mathbf{x}_n) - \widehat{\rho}(\mathbf{x}_0)$ and $\Delta x_n^j = x_n^j - x_0^j$, for $j = 1, 2, 3 \dots D$ as well as $n = 1, 2, 3 \dots D$. Employing this interpolation scheme for each Delaunay cell, then we can straightforwardly produce a continuous space-filling field (i.e., DTFE density field) on a regular grid, which exploits the same anisotropic and self-adaptive scaling features of Delaunay tessellation and guarantees mass conservation, i.e., its volume integral can reproduce the total mass,

$$\widehat{W} = \int \widehat{\rho}(\mathbf{x}) d\mathbf{x} = \sum_{i=1}^N w_i = W = \text{cst.} \quad (10)$$

DTFE in essence is a first-order version of natural neighbour interpolation procedure. Nevertheless, its self-adaptive

nature enables the automatic capture of subtle structural elements in high-density regions with maximum possible resolutions. Meanwhile, it can also properly smooth low-density regions to avoid irritating discreteness. Consequently, DTFE can sharply reconstruct conspicuous structures and hierarchical features of cosmic web from a spatial distribution of sparse tracers, which is of crucial importance to extract maximum amount of morphological information with MFs. In following sections, we will illustrate its compelling performance with quantitative results to highlight the virtues.

4. COSMOLOGICAL N -BODY SIMULATIONS AND DATA SAMPLES

In this work, we adopt two high-resolution pure cold dark matter (DM) N -body simulations for different application requirements. One simulation is dubbed as WMAP_3072_600, which is from the CosmicGrowth simulation suite (Jing 2019), realized by running an adaptive parallel particle-particle-particle-mesh (P³M) N -body code (Jing & Suto 2002; Jing et al. 2007). This simulation incorporates $N_p = 3072^3$ DM particles with mass resolution of $5.5 \times 10^8 h^{-1} M_\odot$ in a periodic cubic box with size of $L = 600 h^{-1} \text{Mpc}$, adopting a WMAP cosmology, i.e., $[\Omega_c, \Omega_b, h, n_s, \sigma_8] = [0.2235, 0.0445, 0.71, 0.968, 0.83]$. The other one is called TianZero simulation (Emberson et al. 2017; Yu et al. 2017), realized by using a publicly-available P³M N -body code CUBEP3M (Harnois-Déraps et al. 2013). This simulation, parameterized with $[\Omega_c, \Omega_b, h, n_s, \sigma_8] = [0.27, 0.05, 0.67, 0.96, 0.83]$, evolves $N_p = 6912^3$ DM particles with mass resolution of $4.6 \times 10^8 h^{-1} M_\odot$ in a cubic box of width $L = 1200 h^{-1} \text{Mpc}$. Both simulations assume flat cosmology, imposing $\Omega_\Lambda = 1 - \Omega_m$, where $\Omega_m = \Omega_b + \Omega_c$.

The WMAP_3072_600 and TianZero are employed to perform DM and halo field level analyses, respectively. As for WMAP_3072_600, in addition to the complete sample of particles (at $z = 0$) with number density of $\bar{n}_p = 1.34 \times 10^2 (h^{-1} \text{Mpc})^{-3}$, we also construct six (10%, 1%, 0.1%, 0.01%, 0.001%, 0.0001%) downgraded particle subsamples produced by random-down-sampling processes without repetition, to study shot noise effects on MFs' measurements. In TianZero, halos are identified by using CUBEP3M's own on-the-fly spherical overdensity (SO) halo finder, which is set to resolve halo masses down to $2.3 \times 10^{11} h^{-1} M_\odot$ with a minimum of 500 particles per halo. Similarly, to investigate the impacts of halo number densities on MFs' measurements, we construct three halo catalogues (at $z = 0.01$) with number densities of $\bar{n}_h = 1.6 \times 10^{-2} (h^{-1} \text{Mpc})^{-3}$, $\bar{n}_h = 1.6 \times 10^{-3} (h^{-1} \text{Mpc})^{-3}$, and $\bar{n}_h = 1.6 \times 10^{-4} (h^{-1} \text{Mpc})^{-3}$, by discarding halos with masses below mass cutoffs of $M_{\min} \simeq 2.3 \times 10^{11} h^{-1} M_\odot$, $M_{\min} \simeq 3.2 \times 10^{12} h^{-1} M_\odot$, and $M_{\min} \simeq 3.1 \times 10^{13} h^{-1} M_\odot$, respectively. The sample selection is chosen due to the consideration that galaxy samples in most observations are determined with faint flux limits (or low mass limits). Note that throughout this paper, subhalos are excluded from analyses.

5. THE MFS OF DM FIELDS

⁶ Here, the subscript n seems to conflict with the previous subscript i . To clarify this confusion for careful readers, we'd like to note that the subscript n used here is only reserved for labelling one of the $D + 1$ vertices of a certain Delaunay cell.

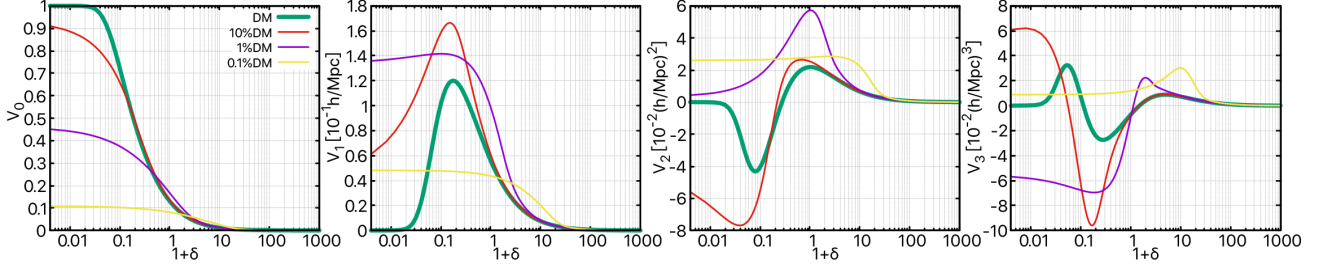


Figure 1. The MFs of noise-free field and 10%, 1%, 0.1% downgraded fields, which are constructed by CIC method with $N_g = 1024^3$ grid cells. They are represented by bold green lines and red, blue, yellow lines, respectively. Here, the bold green lines can be treated as the ideal LSS’s MFs, without discreteness effects. By comparing the lines with different colors, this plot demonstrates how discreteness affects the measurements of MFs.

In this section, we strive to preliminarily demonstrate the superiorities of DTFE method in measuring MFs from sparse tracers. The analyses are performed at matter field level.

5.1. The shot noise effects on MFs

Based on the full and 10%, 1%, 0.1%, 0.01%, 0.001%, 0.0001% downgraded particle samples (cf. Section 4), we construct seven DM fields in real space, by employing a representative mass assignment method, i.e., CIC interpolation. Each field is interpolated on $N_g = 1024^3$ regular grid, with grid cell size $L_g = L/(N_g)^{1/3} \simeq 0.59 h^{-1}\text{Mpc}$,

$$\delta(\mathbf{x}) \equiv \frac{n_p(\mathbf{x})}{\bar{n}_p} - 1, \quad (11)$$

where n_p is particle number density and \bar{n}_p is its mean value. Due to the extremely high particle number density, the DM field constructed from full particle sample can be safely regarded as the underlying noise-free DM field (hereafter noise-free field). The downgraded samples are unbiased samples of the underlying density field, such that the downgraded DM fields (hereafter downgraded fields) can be used to study any pure shot noise effects on MFs. Then, we measure the MFs for each field (hereafter CIC MFs). For simplicity, the results exclusively for the noise-free field and 10%, 1%, 0.1% downgraded fields are presented in Fig. 1.

We find that the shapes of MFs are severely distorted by shot noises. The issue becomes increasingly conspicuous as the particle number density decreases. This is because particles successively become poorer tracers of the underlying DM field, making the downgraded fields choppy (cf. the top panels of Fig. 2). Low-density regions are more vulnerable to the down-sampling process, since shot noises mostly affect these regions. In particular, in poorly sampled regions, with sparse or even no particles, density fields are severely discontinuous or even blank (i.e., $1 + \delta = 0$) (cf. the top panels of Fig. 2). As particle number density decreases, blank regions become larger, thereby the volume fraction of non-zero density regions becomes smaller (cf. the left panel of Fig. 1 and top panels of Fig. 2). Due to the existences of blank regions, the regions with $1 + \delta > 0$ only account for a certain proportion of total box volume (cf. the left panel of Fig. 1). Thus, MFs have step changes⁷, when $1 + \delta = 0 \Rightarrow 1 + \delta > 0$.

⁷ Note that the values of MFs at $1 + \delta = 0$, which respectively are $V_0 = 1$, $V_1 = 0$, $V_2 = 0$, and $V_3 = 0$, cannot be plotted in Fig. 1, because of the logarithmic x-axis.

Moreover, shot noises give rise to various spurious structures on the excursion sets at different density thresholds, depending on down-sampling level. Specifically, for 10% sampling, at low-density thresholds, more and larger isolated under-dense regions (bubbles) are produced by discrete-sampling process, such that V_1 and V_3 become larger and V_2 becomes smaller, relative to the case of noise-free field (the same below). At median density thresholds, we observe a lower negative minimum in V_3 , indicating more porous structures (tunnels), produced by down sampling in the surfaces of excursion sets. As particle number density decreases, downgraded fields will be increasingly dominated by “meatball topology” (i.e., a preponderance of isolated high-density regions). Because of this, for the extreme case of 0.1% sampling, V_2 and V_3 are always positive when $1 + \delta < 1$. For the same case, we see that V_2 and V_3 have higher maximums at high-density thresholds, suggesting that the abundance of isolated regions is increased by breaking up structures into multiple objects as particles are taken out. For the intermediate case of 1% sampling, the corresponding results naturally fall somewhere in between those of the former two cases.

In conclusion, the discreteness effects pose challenges in accurately delineating iso-density contours (i.e., the excursion sets), thereby hindering the proper reflections of intrinsic morphological properties of particle-traced LSS with MFs. Furthermore, in Appendix A, interested readers can find additional results illustrating shot noise effects on MFs with Gaussian smoothing (cf. Kim et al. 2014; Appleby et al. 2017 for genus scenarios).

5.2. The MFs with Gaussian smoothing

Gaussian smoothing with a fixed-kernel size is the most commonly used method to tackle the issue of shot noises (e.g., Park et al. 2005; Choi et al. 2010; Parihar et al. 2014; Kim et al. 2014). In this subsection, to produce continuous fields, we smooth the 1%, 0.1%, 0.01% downgraded fields with Gaussian window functions

$$W(\mathbf{r}) = \frac{1}{(2\pi)^{3/2}R_G^3} \exp\left(-\frac{|\mathbf{r}|^2}{2R_G^2}\right) \quad (12)$$

of smoothing lengths $R_G = 2.93 h^{-1}\text{Mpc}$, $R_G = 5.86 h^{-1}\text{Mpc}$, $R_G = 11.72 h^{-1}\text{Mpc}$, respectively (cf. the middle panels of Fig. 2). Then, we measure the corresponding MFs of these smoothed fields. Hereafter, we refer the MFs measured with this scheme as CIC+GS MFs. The smoothing

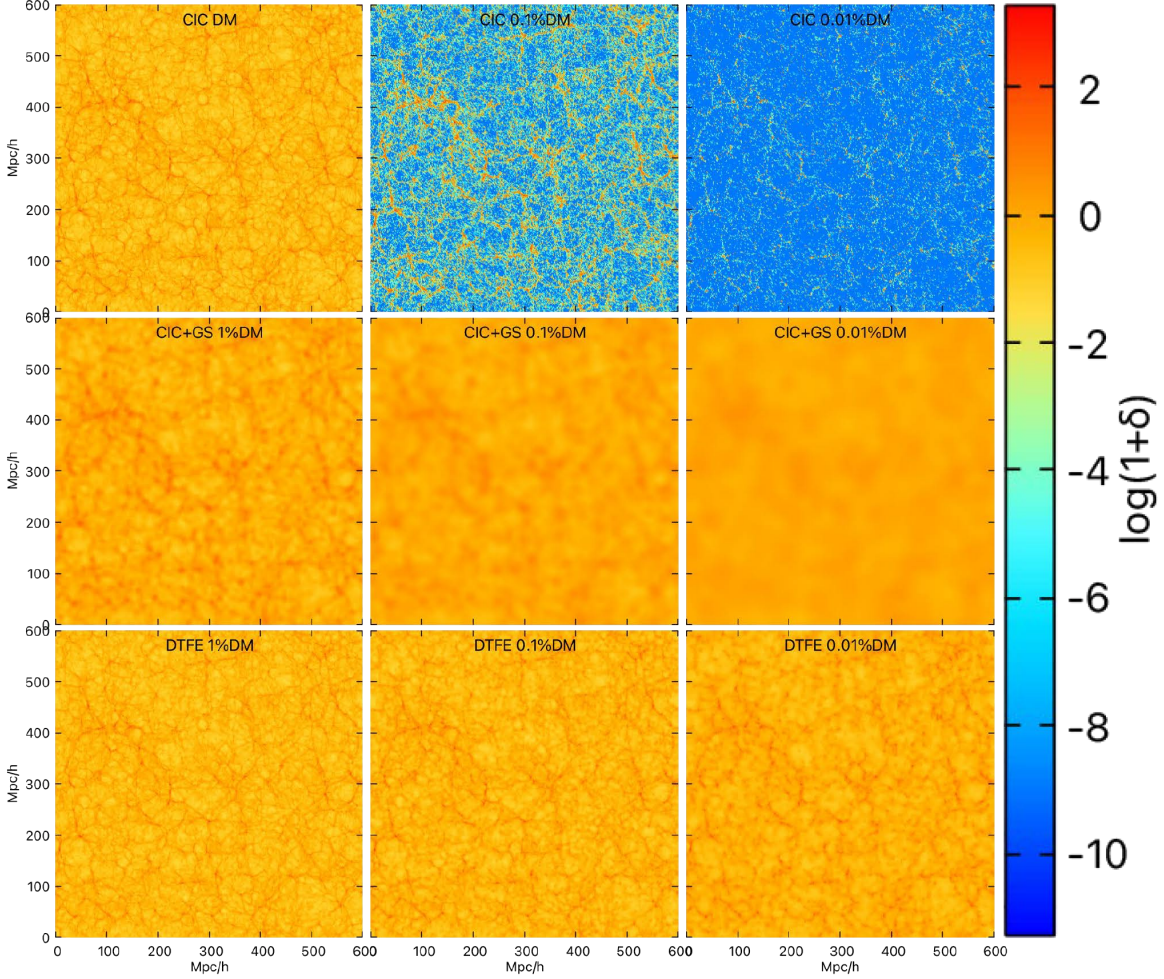


Figure 2. The visualization of two-dimensional slices of downgraded fields constructed by CIC (top), CIC+GS (middle), and DTFE (bottom) methods. As a reference, the noise-free field constructed by CIC method is also presented in the left-top panel. Except for this panel, the left, middle, and right panels represent the 1%, 0.1%, and 0.01% downgraded fields, respectively. All these fields are created by using $N_g = 1024^3$ grid cells within a box of size $L = 600 h^{-1} \text{Mpc}$. Each two-dimensional slice displays the same region of simulation box, with the same projection depth of $5.27 h^{-1} \text{Mpc}$. For CIC+GS case, the smoothing lengths of $R_G = 2.93 h^{-1} \text{Mpc}$, $R_G = 5.86 h^{-1} \text{Mpc}$, and $R_G = 11.72 h^{-1} \text{Mpc}$ are adopted for the 1%, 0.1%, and 0.01% downgraded fields, respectively (cf. Appendix A). In comparison with the left-top panel, the top panels display the emergence of discreteness in CIC DM fields as particle number density is successively downgraded. These severe discreteness effects will hamper proper morphological measurements of LSS with MFs (cf. Fig. 1). The middle panels display the continuous downgraded fields obtained by using CIC+GS method. This method inevitably destroys large amounts of intrinsic structural elements of LSS by introducing excessive smoothing. Therefore, it will significantly diminish the morphological information contents captured by MFs. The bottom panels show the continuous downgraded fields constructed by using DTFE method. Benefiting from the anisotropic and spatial self-adaptive feature, DTFE can help introduce minimum smoothing and retain intrinsic structural elements of LSS to the maximum extent possible. Compared with CIC+GS method, DTFE can greatly improve the morphological information contents captured by MFs (cf. Fig. 3).

lengths adopted here can provide enough smoothing for adequately suppressing discreteness effects without discarding too much structural information (cf. Appendix A for the details of R_G determinations). If smoothing length is too small (e.g., $R_G < \bar{d} \sim \bar{n}_p^{-1/3}$, where \bar{d} is mean tracer spacing), the algorithm may trend to pick out isolated high-density regions (Gott et al. 1987; Gott et al. 1989), leading to the so-called ‘meatball shift’ (cf. Zhang et al. 2010). Actually, the free parameter of R_G is always empirically specified with the requirement of $R_G \geq \bar{d}$. Therefore, the determination of a smoothed field is not unique.

The results for 1% downgraded field are presented in Fig. 3, alongside the CIC MFs of noise-free field serving as references. It seems that CIC+GS method to some degree recovers the shapes of MFs of noise-free field, but showing much lower amplitudes for V_1 , V_2 , and V_3 . The amplitude suppression depends on the adopted smoothing length, i.e., larger smoothing length leading to severer amplitude suppression (cf. Fig. 12). Moreover, after smoothing, MF curves are evidently squeezed towards the direction of intermediate density thresholds (i.e., $1 + \delta \sim 1$), indicating that the smoothed fields become more uniform. This is because the abundance of structural elements is substantially reduced by the smoothing process, significantly diluting intrinsic structures of LSS, especially

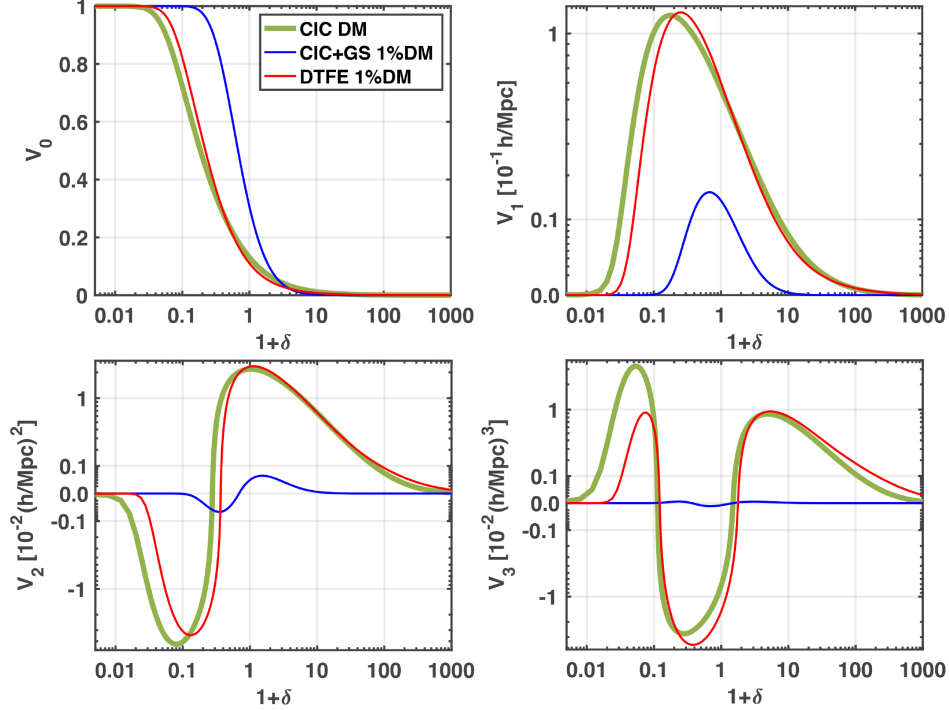


Figure 3. The MFs of noise-free field and two 1% downgraded fields, where the noise-free field is constructed by CIC method, and the two 1% downgraded fields are constructed by CIC+GS and DTFE methods, respectively (cf. Fig. 2). For CIC+GS case, the smoothing length adopted is $R_G = 2.93 h^{-1} \text{Mpc}$. As we can see, the amplitudes of DTFE MFs of 1% downgraded field (i.e., the red lines) are very close to those of CIC MFs of noise-free field (i.e., the bold green lines; also cf. Fig. 1). It means that DTFE indeed can help retain intrinsic structural elements of LSS. While, the amplitudes of CIC+GS MFs (i.e., the blue lines) are much lower than those of MFs in other two cases. This is because CIC+GS scheme erases large amounts of intrinsic structural elements of LSS. Note that these results are plotted with logarithmic y-axis to better visualize the MFs in CIC+GS case.

for strongly clustered regions (cf. the middle panels of Fig. 2). On the other hand, the MFs of smoothed fields approach those of Gaussian random fields, such that they may describe more properties of the Gaussian kernels, than the real morphology of cosmic web (cf. Martínez et al. 2005). Predictably, the recipe of CIC+GS will downgrade the discriminative and constraining powers of MFs in various LSS studies [e.g., neutrino mass effects (Liu et al. 2020), semi-analytic models of galaxy formation (Zhang et al. 2010), etc.], thus limiting its applications.

5.3. The MFs with DTFE

The goal of our efforts is trying to maximize the extractions of true morphological properties with MFs from a set of points. This necessitates an optimal method for reconstructing continuous fields, such that their morphology can faithfully mirror the authentic underlying morphology of the point sets as well as possible. As LSS exhibits a multiscale nature, the smoothing scheme of this method should possess characteristics of anisotropy and spatial self-adaptivity. In fact, these characteristics align precisely with the iconic features of the DTFE method advocated in this paper. Additionally, DTFE also has the virtue of mass conservation and is not reliant on any priori parameters, ensuring the uniqueness of the constructed continuous fields (cf. Section 3). In this subsection, we explore how DTFE method contributes to recovering the morphology of noise-free field from downgraded particle samples.

We construct three DTFE fields with $N_g = 1024^3$ regular grid cells in real space (cf. the bottom panels of Fig. 2), using the same downgraded samples as employed in Section 5.2,

$$\delta_m(\mathbf{x}) \equiv \frac{\hat{\rho}_p(\mathbf{x})}{\bar{\rho}_p} - 1, \quad (13)$$

and then directly measure their corresponding MFs. For comparisons, the results for 1% downgraded field are also presented in Fig. 3. As shown, the shapes of DTFE MFs exhibit noticeable non-Gaussian features, unfolded through the asymmetries of the MF curves. In contrast to CIC+GS MFs, they more closely resemble the MFs of the noise-free field, with much higher amplitudes for V_1 , V_2 , and V_3 . This improvement is attributed to DTFE's capability to resolve a larger number of structural elements from point distribution (cf. the bottom panels of Fig. 2). Nevertheless, these amplitudes are comparatively smaller than those of CIC MFs of the noise-free field, particularly at low-density thresholds, due to the inevitable losses of information⁸. On the other hand, as depicted in Fig. 3, DTFE MFs instead exhibit slightly higher amplitudes at high-density thresholds. This is probably because DTFE can resolve more structural elements in high-density regions, where the impacts of shot noises are less pronounced, than the

⁸ Note that the amplitudes of DTFE MFs will be further suppressed for the cases of downgraded fields with lower particle number densities, resulting from information losses (cf. the bottom panels of Fig. 2 and Section 6.2 for the scenarios of halo fields)

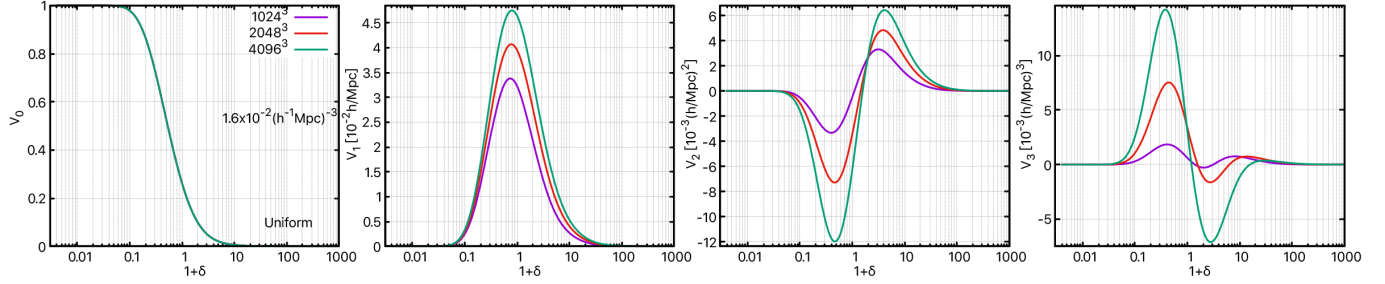


Figure 4. The DTFE MFs of uniform-weighted halo fields with various grid resolutions in real space. The corresponding halo number density for these fields is $1.6 \times 10^{-2} (h^{-1}\text{Mpc})^{-3}$. The blue, red, and green lines correspond to halo fields with $N_g = 1024^3$, $N_g = 2048^3$, and $N_g = 4096^3$ grid cells, respectively. As shown, the amplitudes of V_1 , V_2 , and V_3 become greater as N_g increases. This means that under DTFE scheme, higher grid resolution can help resolve more subtle structural elements from point set.

traditional CIC method. To conclude, these results suggest the great advantages of DTFE method in MFs' measurements, i.e., making morphological information more accessible and ultimately providing strong statistical power (cf. Section 7).

6. SYSTEMATIC EFFECTS ON DTFE MFS OF HALO FIELDS

In realistic data analyses, the measurements of MFs are inevitably affected by many systematic effects. These effects can introduce diverse modifications to the shapes and amplitudes of MFs and should be accurately taken into account to draw any sensible conclusions. Hence, it is theoretically interesting to investigate these systematic effects both analytically and numerically. Previous related works mainly focus on genus statistics (e.g., Park et al. 2005; Kim et al. 2014; Appleby et al. 2017; Melott et al. 1988; Park & Gott 1991; James 2012; Melott & Dominik 1993). In particular, finite pixel (voxel) size effects were analytically studied for 2- (Melott et al. 1989) and 3-dimensional genus (Hamilton et al. 1986); Matsubara & Suto 1996 analytically investigated the RSD effects in linear regime; In weakly non-linear regime, Matsubara 1994 and Matsubara 2003 provided an analytic formula for the effects of non-linear gravitational evolution, which was confirmed by Matsubara & Suto 1996. For MFs, Jiang et al. 2021 recently numerically studied the RSD effects and provided insights into the distinctions in CIC+GS MFs between redshift and real spaces.

Using a state-of-the-art simulation (i.e., TianZero; cf. Section 4), in this section, we investigate various dominant systematic effects on DTFE MFs, which are caused by finite voxel sizes, halo number densities, halo-weighting schemes, and RSDs, with the goal to comprehend how these effects alter the morphological measurements with DTFE MFs. Note that, starting from this section, we perform the analyses for DTFE MFs at halo field level.

6.1. Systematic effects from finite voxel sizes

In the implementation of DTFE, density field is ultimately sampled on a regular grid (cf. Section 3), which effectively eliminates the adaptive nature of DTFE below the scale of voxel size. As grid becomes coarser, certain fine-scale or faint structures of cosmic web (e.g., substructures of voids, small filamentary features, etc.) tend to be insufficiently resolved. This deficiency will result in the amplitude drops for V_1 , V_2 , and V_3 (cf. Kim et al. 2014 and Appleby et al. 2017

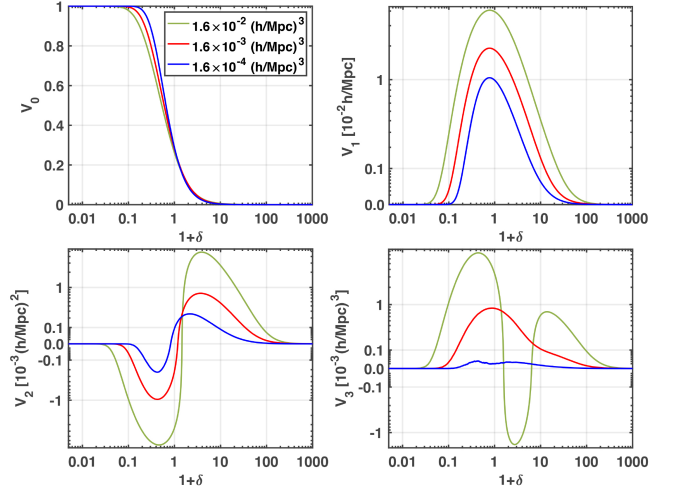


Figure 5. The DTFE MFs of uniform-weighted halo fields with various halo number densities in real space. The green, red, and blue lines correspond to halo number densities of $1.6 \times 10^{-2} (h^{-1}\text{Mpc})^{-3}$, $1.6 \times 10^{-3} (h^{-1}\text{Mpc})^{-3}$, and $1.6 \times 10^{-4} (h^{-1}\text{Mpc})^{-3}$, respectively. The amplitudes of MFs decrease with the decrease of halo number density, indicating information losses in lower halo number density cases.

for the scenario of genus with Gaussian smoothing), irrespective of halo number densities, weighting schemes (cf. Section 6.3), etc. We demonstrate it in Fig. 4, where DTFE MFs are measured from halo fields in real space with grid resolutions of $N_g = 4096^3$, $N_g = 2048^3$, and $N_g = 1024^3$ (corresponding to voxel sizes of $0.586 h^{-1}\text{Mpc}$, $0.293 h^{-1}\text{Mpc}$, and $1.171 h^{-1}\text{Mpc}$), respectively. Here, we employ the case of uniform weighting with $\bar{n}_h = 1.6 \times 10^{-2} (h^{-1}\text{Mpc})^{-3}$ to quote our results. In essence, the finite voxel size effects (i.e., smoothing effects cause by grid window) are entirely numerical artifacts, which should be minimized by adopting sufficiently large grid sizes while keeping acceptable memory overheads. In the following, we choose $N_g = 2048^3$ to construct halo fields.

6.2. Systematic effects from halo number densities

In observation, the morphological properties of LSS can only be measured from biased tracers. The situation becomes more complicated due to the entanglement between the effects of shot noise and halo/galaxy bias, as compared with the case

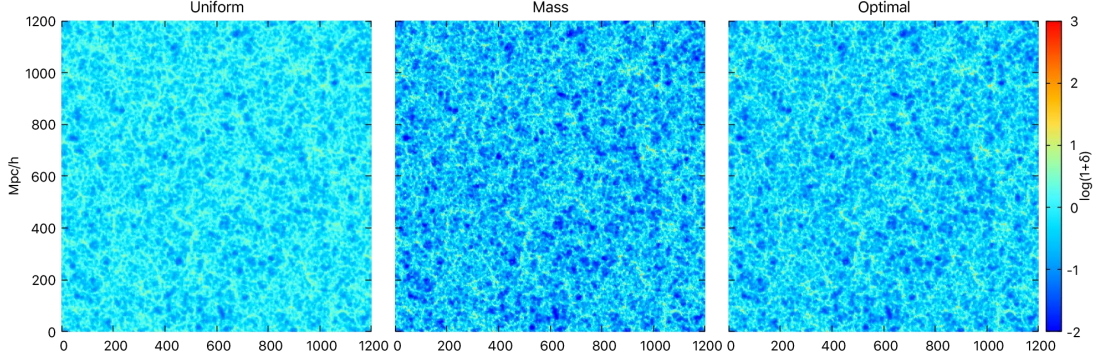


Figure 6. The visualization of two-dimensional slices of different weighted DTFE halo fields in real space. The corresponding halo number density for these fields is $1.6 \times 10^{-2} (h^{-1}\text{Mpc})^{-3}$. From left to right, each panel corresponds to uniform-, mass-, and optimal-weighted halo field, respectively. Each slice shows the same $1200 \times 1200 (h^{-1}\text{Mpc})^2$ region with $10.55 h^{-1}\text{Mpc}$ thickness of the simulation box.

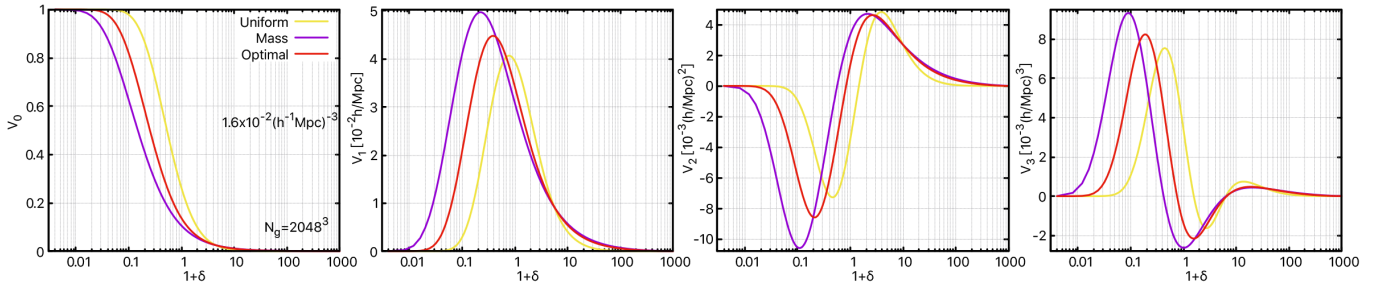


Figure 7. The DTFE MFs of various weighted halo fields (cf. Fig. 6) in real space. The corresponding halo number density for these fields is $1.6 \times 10^{-2} (h^{-1}\text{Mpc})^{-3}$. The yellow, blue, and red lines are for the uniform-, mass-, and optimal-weighted halo fields, respectively.

of matter field (cf. Section 5). In our study, it is quite non-trivial to separate these two effects, as the effective masses of our halo samples, which essentially determine the biasing effects⁹, have intrinsic relations with halo number densities. On the other hand, certain degrees of smoothness are also inevitably introduced in DTFE fields due to the limited halo number densities, which determine the effective smoothing lengths of the sophisticated DTFE windows. Therefore, the systematic effects caused by halo number density are actually combined effects jointly determined by halo bias, shot noise, and DTFE smoothing.

To investigate the combined effects, we measure DTFE MFs of uniform-weighted halo fields in real space constructed from halo samples with different number densities. The results are presented in Fig. 5. We note that these effects are the strongest effects within our tested domain. As observed, a reduction in halo number density results in the compression of MFs along the $1 + \delta \sim 1$ direction and leads to lower amplitudes for V_1 , V_2 , and V_3 . This occurs because lower halo number densities induce larger smoothing effects, producing smaller root-mean-square (r.m.s) values of densities. Additionally, the decrease in halo number density also makes the halos less effective as tracers of the underlying matter field, naturally leading to the losses of intrinsic structural information of LSS. In particular, when halo number density becomes sufficiently

low (e.g., the case of $\bar{n}_h = 1.6 \times 10^{-4} (h^{-1}\text{Mpc})^{-3}$), V_3 is consistently nonnegative across all density thresholds (i.e., $V_3 \geq 0$ for $1 + \delta \in (0, +\infty)$), which indicates that the halo field is dominated by structures of isolated objects (i.e., ‘meatball’ structures).

6.3. Systematic effects from halo-weighting schemes

DTFE halo fields can be constructed under different halo weightings (cf. Section 3), which can yield different halo biases (Liu et al. 2021). In this work, we consider three weighting schemes: uniform, mass (Seljak et al. 2009), and optimal¹⁰ (Hamaus et al. 2010; Cai et al. 2011) weightings, represented by the forms $w_i(M) = 1, M_i, M_i + M_0$, respectively. Here, M_0 is a free parameter, and we adopt $M_0 = 3M_{\min}$ ¹¹ (Hamaus et al. 2010), where M_{\min} is the mass cutoff (cf. Section 4). Since the last two weightings both depend on halo masses, we collectively denote them as mass-dependent weightings. These two weightings have been utilized in various cosmological studies [e.g., primordial non-Gaussianities (Hamaus et al. 2011), growth rate of structure formation (Hamaus et al. 2012), and initial condition reconstruction (Liu et al. 2021), etc.], given that they can significantly improve the correlation between halo field and

⁹ It should be theoretically intriguing to explore ‘morphological bias’ by analyzing MFs of halo samples within different mass bins (cf. the ‘topological bias’ found in Bermejo et al. 2024). As this falls outside the scope of this paper, systematic studies are left for future research.

¹⁰ The ‘optimal weighting’ refers to the weighting scheme that can minimize the stochasticity of halos with respect to underlying dark matter (Hamaus et al. 2010; Cai et al. 2011; Liu et al. 2021).

¹¹ Note that this is an empirical relation found in Hamaus et al. 2010, which may not hold under a different condition, e.g., using a different halo-finder algorithm (cf. Liu et al. 2021). Here, we just naively employ this relation as a proxy for the optimal weighting in our tests.

underlying matter field (cf. Seljak et al. 2009; Hamaus et al. 2010; Liu et al. 2021).

Compared to uniform weighting, mass-dependent weightings tend to upweight the regions with higher halo abundance, as these regions are more likely to contain massive halos (cf. Haas et al. 2012; Zhao et al. 2015). As a result, the density contrasts between high- and low-density regions are intensified in mass-dependent weighted halo fields, leading to the stretching of corresponding MFs in two opposite directions (cf. Fig. 6 and Fig. 7). Also, due to halo fields being dominated by low-density regions, the MFs of mass-dependent weighted halo fields are visually shifted towards the direction of low-density thresholds. Moreover, we observe that the amplitudes of V_1 , V_2 , and V_3 for mass-dependent weightings are enhanced relative to the case of uniform weighting. This implies that mass-dependent weightings presumably aid in resolving more structural elements when estimating halo fields, consistent with previous findings that mass information can enhance the correlation between halo field and underlying matter field (Seljak et al. 2009; Hamaus et al. 2010; Liu et al. 2021).

6.4. Systematic effects from RSDs

In galaxy surveys, LSS is actually mapped in redshift space, where the positions of galaxies are misrepresented due to peculiar velocities, induced by gravitational field, along the line of sight (LOS). This phenomenon is referred to as redshift space distortions (RSDs). The RSDs blur density field in redshift space, leading to a striking anisotropic feature in the direction of LOS. On larger scales, coherent infall of galaxies produces squashed pancake-like distortions, known as Kaiser’s effect (Kaiser 1987). Whereas, on smaller scales, peculiar velocities of bound objects tend to generate elongated structures, known as fingers-of-God (FOG) effect (Jackson 1972). In cosmology, these effects provide a generic way to probe peculiar velocity field, and are commonly used to measure the growth rate of structure formation.

To investigate the effects of RSDs on DTFE MFs, we compute the MFs of uniform-weighted halo fields with $\bar{n}_h = 1.6 \times 10^{-2} (h^{-1}\text{Mpc})^{-3}$ separately in real and redshift space (cf. Fig. 8). In redshift space, the distant-observer approximation is adopted to obtain halo positions,

$$\mathbf{s} = \mathbf{r} + \frac{(1+z)\mathbf{v}_{\parallel}}{H(z)}, \quad (14)$$

where \mathbf{r} , z , \mathbf{v}_{\parallel} , and $H(z)$ is the halo position in real space, redshift, LOS component of halo peculiar velocity, and Hubble parameter, respectively. We observe that in redshift space, all curves of MFs are stretched in two opposite directions compared to their counterparts in real space, indicating that RSD effects increase the r.m.s values of densities (Jiang et al. 2021). Nevertheless, the main effect of RSDs is the decrease in amplitudes of V_1 , V_2 , and V_3 .

Since valuable information about velocity field is encoded in RSD effects, an accurate modelling for these effects on MFs would open up a unique window to extract information on structure growth rate. In linear regime, Matsubara 1996 found that Kaiser’s effect on genus (equivalent to V_3) can be

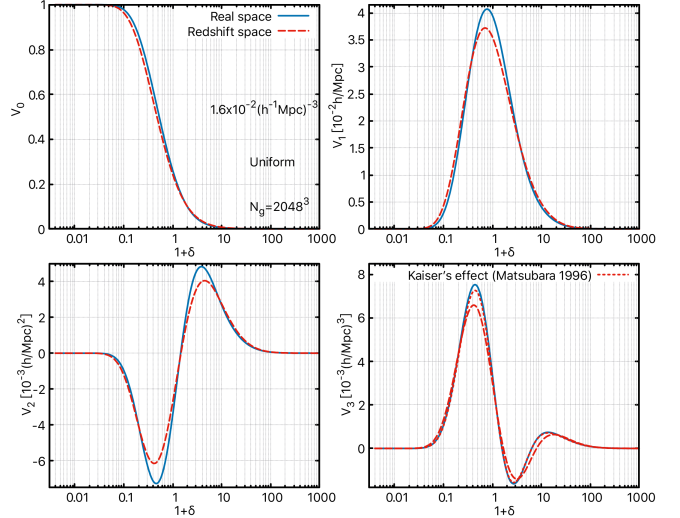


Figure 8. The DTFE MFs of uniform-weighted halo fields in real space and redshift space. The corresponding halo number density for these fields is $1.6 \times 10^{-2} (h^{-1}\text{Mpc})^{-3}$. The solid and dashed lines represent the MFs in real and redshift space, respectively. As a reference, V_3 with linear Kaiser’s effect is also plotted (cf. the dotted line). As shown, the main RSD effect on MFs is the reduction in amplitudes of V_1 , V_2 , and V_3 .

predicted by

$$G^{(z)}(v) = \frac{3\sqrt{3}}{2} \sqrt{C} (1-C) G^{(r)}(v), \quad (15)$$

where $G^{(z)}(v)$ and $G^{(r)}(v)$ is the genus in redshift and real space, respectively. The parameter C is expressed as

$$C = \frac{1}{3} \frac{1 + \frac{6}{5}fb^{-1} + \frac{3}{7}(fb^{-1})^2}{1 + \frac{2}{3}fb^{-1} + \frac{1}{5}(fb^{-1})^2}. \quad (16)$$

Here, b is the halo/galaxy bias, and f is the dimensionless linear growth rate, defined as

$$f \equiv \frac{d \ln D}{d \ln a} \approx \Omega_m^{4/7} + \frac{\Omega_\Lambda}{70} \left(1 + \frac{\Omega_m}{2}\right), \quad (17)$$

where D is the linear growth factor, and a is the expansion parameter (Lahav et al. 1991; Hamilton 2001). Equation (15) suggests that the extent of amplitude decline caused by RSDs depends on growth rate and halo/galaxy bias, such that this effect can be utilized to constrain these cosmological parameters.

DTFE MFs can naturally capture non-linear structure formation signatures induced by FOG effect. This is because DTFE tends to preserve maximum amount of non-linear structures, which are typically smoothed out in the CIC+GS scheme with a large R_G (cf. Kim et al. 2014 and Appleby et al. 2022 for (quasi-) linear-scale scenarios). Therefore, our results do not fit well with linear theory predictions (e.g., the Equation (15) under Kaiser approximation; also cf. Fig. 8). Indeed, using N -body simulations, Matsubara & Suto 1996 found that the amplitude of genus is more suppressed than

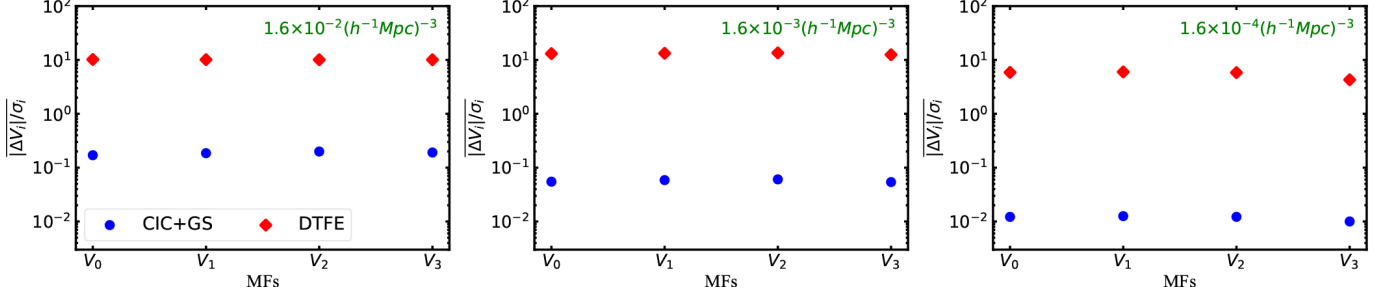


Figure 9. The mean RSD S/N ratios. They are obtained by taking the average of $|\Delta V_i|/\sigma_i$ (cf. Fig. 13) in density threshold range of $[0.003, 1000]$, i.e., $|\Delta V_i|/\sigma_i$. The results for CIC+GS and DTFE MFs are marked with blue circles and red diamonds, respectively. As shown, the y-axis values of red diamonds are much higher than those of blue circles by around 2 orders of magnitude. This means that the discriminative power of DTFE MFs for RSD effects is much stronger than that of CIC+GS MFs.

expected by linear theory (also cf. Kim et al. 2014), consistent with our results (cf. the bottom-right panel of Fig. 8). Nevertheless, in principle, we can still apply emulator-based approaches to parameter estimates (cf. Marques et al. 2019; Petri et al. 2015), where significant RSD signatures should be critical to improving constraining power of MFs on cosmological parameters. This subject is beyond the scope of this work, and we defer the investigations to future studies.

7. THE STATISTICAL POWER OF DTFE MFs IN EXTRACTING COSMOLOGICAL INFORMATION

In this section, we proceed to illustrate the strong statistical power of DTFE MFs in extracting cosmological information. For practical purposes, we restrict our analyses to extracting the cosmological information encoded in RSDs. Similar to Section 5, we also present the results of CIC+GS MFs as references for comparisons, but with a different strategy for determining smoothing lengths. Here, the smoothing lengths are determined by the mean halo spacing, i.e., $\bar{d} \sim \bar{n}_h^{-1/3}$. For our halo samples with number densities in descending order, they are $R_G = 6.8 h^{-1} \text{Mpc}$, $R_G = 14.6 h^{-1} \text{Mpc}$, and $R_G = 31.4 h^{-1} \text{Mpc}$, respectively. Note that these smoothing lengths are traditionally regarded as the smallest smoothing lengths that can be employed for CIC+GS MFs. Therefore, the comparative results displayed in this section are relatively conservative.

7.1. The discriminative power for RSDs

In this subsection, we quantitatively assess the discriminative power of DTFE MFs for RSD effects. To this end, we calculate the differences in MFs of uniform-weighted halo fields with various number densities between real and redshift space,

$$\Delta V_i(\nu) = V_i^{(z)}(\nu) - V_i^{(r)}(\nu), \quad (18)$$

where $V_i^{(r)}(\nu)$ and $V_i^{(z)}(\nu)$, with $i = 0, 1, 2, 3$, represent the MFs in real and redshift space, respectively. The results are shown in Fig. 13, where the error bars are obtained by

$$\sigma = \sqrt{\sigma_z^2 + \sigma_r^2}. \quad (19)$$

Here, σ_z and σ_r denote the errors of MFs (cf. Section 2) in real and redshift space, respectively.

We see that, for V_1 , V_2 , and V_3 , RSD signals in DTFE MFs are significantly higher than those in CIC+GS MFs, regardless

of halo number density. And, our results are well consistent with those found in previous works (e.g., Kim et al. 2014; Jiang et al. 2021; Lippich & Sánchez 2021; Appleby et al. 2022), but showing more pronounced signals in DTFE case. Moreover, intriguingly, despite our analyses being performed at halo field level, we find that the signs and trends of $\Delta V_i(\nu)$ in our work are broadly the same as those in Jiang et al. 2021, where CIC+GS DM fields were employed for analyses. For interpretations of $\Delta V_i(\nu)$, we refer interested readers to that paper to find more details. In Fig. 13, we also present the S/N ratios of RSD effects, defined as $|\Delta V_i|/\sigma_i$. As shown, the amplitudes of RSD S/N ratios for DTFE MFs are also larger than those for CIC+GS MFs, except for $|\Delta V_0|/\sigma_0$ with $\bar{n}_h = 1.6 \times 10^{-2} (h^{-1} \text{Mpc})^{-3}$ (cf. the bottom subplot in left-top panel of Fig. 13), where the amplitudes in the two cases are basically comparable.

In fact, comparing S/N ratio amplitudes is not an effective way for assessing the relative performance of these two methods in extracting RSD signals. A more suitable approach is to compare the areas between the S/N curves and the x-axis. For this reason, we calculate the mean RSD S/N ratios, which are defined as

$$\overline{|\Delta V_i|/\sigma_i} \equiv \frac{\int_{\nu_{\min}}^{\nu_{\max}} |\Delta V_i|/\sigma_i}{\nu_{\max} - \nu_{\min}}, \quad (20)$$

where $\nu_{\min} = 0.003$ and $\nu_{\max} = 1000$. Note that the numerator on the right-hand side of Equation (20) is exactly the area between the S/N curve and the x-axis within the range of $[\nu_{\min}, \nu_{\max}]$. The results are shown in Fig. 9. Expectedly, DTFE leads to remarkable improvements over CIC+GS in terms of discriminative power for RSD effects, by ~ 2 orders of magnitude (cf. Fig. 9). Unquestionably, this is because DTFE MFs are more informative and thus more sensible to any modifications in halo fields.

Additionally, due to information losses, $|\Delta V_i|/\sigma_i$ becomes lower as halo number density decreases, regardless of the schemes for measuring MFs. In particular, when halo number density becomes too low, halo fields will be dominated by structures of isolated objects, making the intrinsic topologies of these structures less susceptible to the deformations caused by RSDs (cf. Fig. 13 and Fig. 9). On the other hand, we also notice a somewhat counter-intuitive result, i.e., for DTFE MFs with $\bar{n}_h = 1.6 \times 10^{-3} (h^{-1} \text{Mpc})^{-3}$, $|\Delta V_i|/\sigma_i$ is instead higher than that of the case with $\bar{n}_h = 1.6 \times 10^{-2} (h^{-1} \text{Mpc})^{-3}$. This

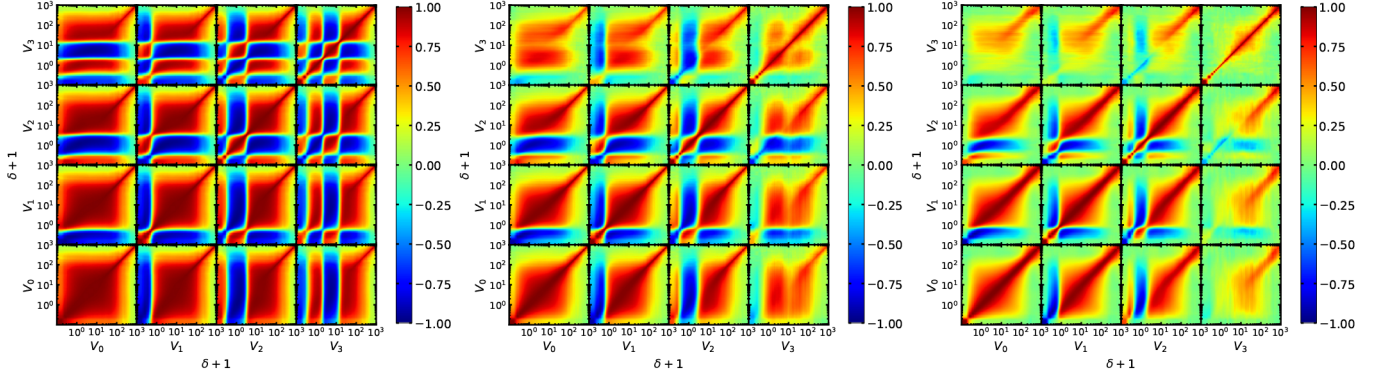


Figure 10. The correlation matrices for DTFE MFs of uniform-weighted halo fields with different number densities. From left to right, each panel shows the case of halo number density of $1.6 \times 10^{-2} (h^{-1}\text{Mpc})^{-3}$, $1.6 \times 10^{-3} (h^{-1}\text{Mpc})^{-3}$, and $1.6 \times 10^{-4} (h^{-1}\text{Mpc})^{-3}$, respectively.

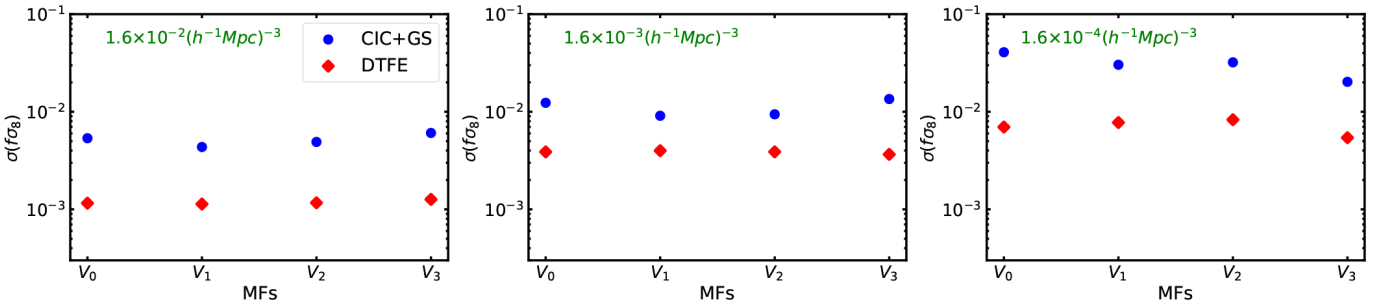


Figure 11. The Fisher error forecasts for structure growth rate, with $n_b = 32$ (cf. Section C for technical details). The results for CIC+GS and DTFE MFs are marked with blue circles and red diamonds, respectively. As shown, the y-axis values of red diamonds are much lower than those of blue circles by a factor of around 3-5. This means that compared with traditional CIC+GS MFs, DTFE MFs are more sensitive to cosmological parameters, because they contain more morphological information of LSS.

may be caused by data truncation effect: density thresholds are limited to $[0.003, 1000]$ in our calculation, while there are still RSD signals above $\nu = 1000$ (cf. Fig. 13); for larger \bar{n}_h , DTFE MFs could have captured signals from higher-density regions, but more signals were abandoned. As for CIC+GS MFs, they do not suffer from such data truncation effect, so their corresponding results appear rational.

7.2. The constraining power on structure growth rate

In the analyses of last subsection, we actually ignore the correlations between data points at different density thresholds. However, in reality, the correlations do exist and are quite significant. This can be seen from Fig. 10, where correlation matrices for DTFE MFs of uniform-weighted halo fields under various number densities are presented. One can observe that the correlation matrices exhibit certain regular patterns. By comparing Fig. 5 and Fig. 10, we notice that the data points on MF-curve segments with same trend are positively correlated, while the data points on rising MF-curve segments are negatively correlated with those on falling MF-curve segments.

In this subsection, by taking into account these correlations, we go a step further to investigate the sensitivities of DTFE MFs to cosmological parameters, i.e., the constraining power. As a case study, we conduct simple Fisher forecasts for the errors on structure growth rate $f\sigma_8(z = 0.01)$, a key cosmological parameter often constrained in RSD studies (cf. Appendix C for technical details). Here, σ_8 is the amplitude

of density fluctuations within a sphere of comoving radius $R = 8 h^{-1}\text{Mpc}$, which can be obtained by

$$\sigma_8^2 = \frac{1}{2\pi^2} \int P_m(k) |W(kR)|^2 k^2 dk, \quad (21)$$

where

$$W(kR) = \frac{3[\sin(kR) - kR \cos(kR)]}{k^3 R^3} \quad (22)$$

is the top-hat window function in Fourier space and $P_m(k)$ is the matter power spectrum. In this study, Fisher forecasts are performed for each $V_i(\nu)$, under various halo number densities, and the results are shown in Fig. 11.

As shown, the predictive errors increase with the decrease in halo number densities, attributed to information losses. In particular, DTFE MFs yield much stronger constraining power, exhibiting remarkable improvement by a factor of $\sim 3-5$ over CIC+GS MFs within our tested domain. The results unequivocally demonstrate that DTFE MFs outperform traditional CIC+GS MFs in constraining cosmology. Again, this is due to the fact that DTFE MFs can capture more morphological information of LSS from halo distribution. In Fig. 11, the results are obtained by utilizing V_i with 32 data points. For consistency check, we also employ V_i with 64 data points for Fisher forecasts (cf. Fig. 15). The results from both approaches are consistent, and they are specific to the survey volume of our simulation box, i.e., $1.728 (h^{-1}\text{Gpc})^3$. If volume increases, the predictive errors will be further reduced. It

is noteworthy that various numerical and observational systematic effects (e.g., data selection, irregular survey mask, and those investigated in Section 6) can affect the predictions, but hard to change our conclusions.

8. SUMMARIES AND DISCUSSIONS

In cosmology, constructing density fields from point sets is a basic task to perform grid-based analyses of LSS. The choice of a particular method is often a compromise between desired field properties and limitations of the method. In particular, constructing continuous fields is essential to specify iso-density surfaces for estimating MFs. To achieve this, traditional mass assignment methods typically require tracer samples with high number densities to ensure sufficient sampling per grid cell. Otherwise, poorly sampled under-dense regions will be dominated by prominent shot noises, severely limiting their applicabilities to sparse datasets. Therefore, these methods are always utilized in conjunction with smoothing recipes at the cost of erasing substantial structural information. It is obviously not an optimal solution because the ultimate goal should be to preserve the intricate LSS multi-scale patterns as faithfully as possible. A significant advancement toward this objective can be attained by leveraging DTFE technique, which can produce piece-wise continuous fields with unique features of being parameter-free, self-adaptive in scale, and preserving mass conservation.

In this work, we propose to optimize the extractions of morphological information from cosmic web tracers with DTFE MFs. We perform systematic analyses in a step-by-step manner, starting from matter field level and progressing to halo field level:

- At matter field level, we first investigate shot noise effects on CIC MFs, elucidating the challenges posed by severe discreteness in the density fields, constructed by traditional mass assignment methods, for proper morphological measurements from sparse tracers with MFs. Then, we measure CIC+GS MFs (i.e., the traditional scheme) and DTFE MFs (i.e., the new scheme) from the same downgraded particle samples and compare them to preliminarily demonstrate the superiorities of DTFE method in measuring MFs from point sets. For CIC+GS MFs, we explore the corresponding shot noise effects and propose a strategy for determining smoothing lengths to sufficiently eliminate shot noises without excessively erasing structural information.
- At halo field level, we first numerically study various dominant systematic effects on DTFE MFs, induced by finite voxel sizes, halo number densities, halo-weighting schemes, and redshift space distortions. Then, we showcase the robust statistical power of DTFE MFs for extracting cosmological information encoded in RSDs. We find that DTFE MFs remarkably outperform traditional CIC+GS MFs by ~ 2 orders of magnitude in discriminative power for RSD effects and by a factor of $\sim 3-5$ in constraining power on structure growth rate. This is because DTFE scheme can help conserve maximum morphological information of LSS from sparse tracers, rendering DTFE MFs more sensitive to cosmological parameters.

In view of the strong statistical power of DTFE MFs, we will employ this method to extract various critical cosmological signatures [e.g., neutrino masses (Liu et al. 2020), modified gravities (Fang et al. 2017), and primordial non-Gaussianities (Hikage et al. 2006; Hikage et al. 2008)] imprinted on halo/galaxy fields, in our ongoing projects.

The implementation scheme for measuring MFs proposed in this paper is conceptually related to other Delaunay-based methods developed in previous works (Aragon-Calvo et al. 2010; Lippich & Sánchez 2021). These works compute MFs from triangulated iso-density surfaces, which are directly specified from Delaunay tessellation of a point set, without interpolating density field onto a regular grid. When density values at tessellation vertexes in these methods are estimated in the same manner as DTFE, their performance in measuring MFs should be highly similar to that of our method, with an added advantage of being free from finite voxel size issue. Alternatively, there might also be a possibility to directly evaluate MFs from alpha shapes of discrete tracers, which are specified via filtrations of Delaunay tessellation (van de Weygaert et al. 2011). Despite all that, the method presented in this work stands out for its simplicity and convenience in implementation, as it does not require any additional complex code designs for extracting MFs from triangulated isosurfaces. This is undeniably one of the main merits of our method.

Moreover, It's well-known that Delaunay-based methods are sensitive to point perturbations, leading to substantial rearrangements in Delaunay tessellation. These methods also tend to produce prominent undesired spike-like artifacts due to highly elongated tetrahedra, which hinders the accurate identification of faint structures in point distribution. These issues seem still to be particularly problematic for morphological studies of LSS. One potential solution¹² to address these concerns is the use of an ensemble-based DTFE technique (Aragon-Calvo 2021). This method computes the mean DTFE field from an ensemble of point realizations by perturbing the original point set following geometric constraints. It can be regarded as a natural generalization of DTFE and shares the same advantageous characteristics of DTFE. Therefore, the measurements of MFs with ensemble-based DTFE can be easily implemented on top of our method and merit investigations in future studies.

ACKNOWLEDGMENTS

Y.L. would like to thank Cheng Zhao, Charling Tao, Yuting Wang, Shuo Yuan, Zhao Chen, Zhengxiang Li, and Dandan Xu for useful communications. We also thank the anonymous referee for their very detailed and helpful comments, which helped make the paper more informative. This work was supported by National Science Foundation of China (Nos. 12303005, 12273015, 12273020, 11621303, 12173030), National Key R&D Program of China (Nos. 2023YFA1605601,

¹² Recently, Feldbrugge 2024 proposed a phase-space DTFE (PS-DTFE), a hybrid method trying to combine advantages of phase-space density estimator (Shandarin et al. 2012; Abel et al. 2012) and DTFE. However, PS-DTFE field exhibits discontinuities at fold caustic surfaces. And, it also relies on prior knowledge of tracers before shell crossing, limiting its feasibility to simulated data.

2023YFA1607800, 2023YFA1607802), and the science research grants from China Manned Space Project with No. CMS-CSST-2021-A03. Y.L. acknowledges support from Shuimu Tsinghua Scholar Program (No. 2022SM173). Y.Y.

acknowledges the sponsorship from Yangyang Development Fund. This work made use of the Gravity Supercomputer at the Department of Astronomy, Shanghai Jiao Tong University.

APPENDIX

A. THE DETERMINATIONS OF SMOOTHING LENGTHS

In this appendix, we illustrate our strategy for determining the smoothing lengths adopted in Section 5.2 and display the effects of shot noise on CIC+GS MFs. In previous works (e.g., Park et al. 2005; Choi et al. 2010; Parihar et al. 2014; Kim et al. 2014), smoothing lengths were empirically determined with the restriction $R_G \geq \bar{d} \sim \bar{n}_{\text{tracer}}^{-1/3}$, where \bar{n}_{tracer} is tracer number density. Actually, in our tests, setting $R_G = \bar{d}$ cannot provide adequate smoothing for completely eliminating shot noise effects. Our strategy is to strike a balance between removing shot noise effects and retaining sufficient information. To achieve this, R_G is determined through an iterative and stepwise refined process, such that the differences of MFs between downgraded field and noise-free field are controlled within $1\text{-}\sigma$ deviation. We note that this strategy seems to have never been proposed before. Therefore, it is worth exploring it theoretically.

The results are visualized in Fig. 12, where MFs of noise-free field and three successive downgraded fields adopt the same R_G for each column. It explicitly illustrates the specified smoothing lengths, i.e., $R_G = 2.93 h^{-1}\text{Mpc}$, $R_G = 5.86 h^{-1}\text{Mpc}$, and $R_G = 11.72 h^{-1}\text{Mpc}$ for the 1%, 0.1%, and 0.01% downgraded fields, respectively. Meanwhile, we can also see that shot noises characteristically make the amplitudes of V_1 , V_2 , and V_3 increase (cf. Kim et al. 2014) and result in MF curves being stretched in two opposite directions. This is because discrete effects generate more pseudo structures on excursion sets, leading to choppier density fields with larger r.m.s of densities. This process for R_G determinations would also be applicable to the cases of halo fields. In consideration that it is not the main concern of our paper, we leave the systematic investigations on this topic to future investigations.

B. THE RSD SIGNALS AND S/N RATIOS EXTRACTED FROM DTFE MFS

In this appendix, we provide the RSD signals (cf. Equation 18) and the associated RSD S/N ratios extracted from DTFE MFs (cf. Section 7.1). The results are shown in Fig. 13. The figure is decided to be displayed here due to its large size as well as the fact that the main information it conveys is already effectively presented in Fig. 9.

C. THE METHODOLOGY OF FISHER FORECASTS FOR ERRORS ON STRUCTURE GROWTH RATE

In our work, Gaussian likelihood is assumed, and the dependence of covariance matrix on model parameters is also ignored. Therefore, the elements of Fisher matrix F can be written as

$$F_{\alpha\beta} = \frac{\partial \boldsymbol{\mu}^T}{\partial \theta_\alpha} \mathbf{C}^{-1} \frac{\partial \boldsymbol{\mu}}{\partial \theta_\beta}, \quad (\text{C1})$$

where α and β label the parameters of interest, $\boldsymbol{\mu}$, $\boldsymbol{\theta}$, and \mathbf{C} are the mean of data vector \mathbf{x} , vector of model parameters, and data covariance matrix, respectively (cf. Euclid Collaboration et al. 2020). The elements of \mathbf{C} are computed as

$$C_{ij} = \sum_{r=1}^N \frac{(x_i^r - \mu_i)(x_j^r - \mu_j)}{N-1}, \quad (\text{C2})$$

where $\mu_{i(j)} = \sum_r x_{i(j)}^r / N$, $i(j) = 1, 2, 3 \dots n_b$, r represents the r -th data realization, N and n_b denote the number of data realizations and number of data vector elements, respectively. Furthermore, we rescale the inverse covariance matrix \mathbf{C}^{-1} with a factor $(N - n_b - 2)/(N - 1)$ to correct for the bias induced by finite number of data realizations¹³ (Hartlap et al. 2007). Finally, the diagonal element of the inverse of Fisher matrix $(\mathcal{F})_{ii}^{-1}$ yields the lower limit to the error of i -th model parameter (marginalized over other parameters),

$$\sigma_{\theta_i}^2 \geq (\mathcal{F})_{ii}^{-1}. \quad (\text{C3})$$

In our scenario, data vectors refer to the MFs in redshift space $V_i^{(z)}(\nu)$, and data realizations refer to the $V_i^{(z)}(\nu)$ measured from $n_f = 8^3 = 512$ subfields (cf. Section 2). Specifically, the covariance matrices are first calculated by using the 512 subfields with RSDs and then are rescaled by $1/n_f$ ¹⁴. To calculate the derivatives in Equation C1, we construct two additional halo fields with modified RSDs by artificially increasing and decreasing the peculiar velocity of each halo by a factor of 0.03, respectively. Then, the response functions are given as $\Delta \boldsymbol{\mu} = \boldsymbol{\mu}_{v_+} - \boldsymbol{\mu}_{v_-} = \Delta V_i^{(z)}(\nu)$, where subscripts v_+ and v_- indicate the two cases of increasing and decreasing halo peculiar velocities, respectively. Moreover, in RSD studies, there is an approximate relational expression between structure growth rate $f\sigma_8(z)$ and halo/galaxy velocity bias b_v (cf. Chen et al. 2018),

$$\left. \frac{\delta(f\sigma_8)}{f\sigma_8} \right|_{k,z} \simeq - \left. \frac{\delta b_v}{b_v} \right|_{k,z}. \quad (\text{C4})$$

Therefore, in our scenario, the change in $f\sigma_8$ can be expressed as $\Delta(f\sigma_8) \simeq -\frac{\Delta b_v}{b_v} f\sigma_8 = -\frac{b_{v_+} - b_{v_-}}{b_v} f\sigma_8 = -0.06 f\sigma_8$. At this

¹³ The validity of this correction assumes Gaussian errors and uncorrelated data vectors. This is not strictly true for most scenarios. To minimize impacts of this assumption, N needs to be sufficiently larger than n_b .

¹⁴ This method is based on an implicit assumption that all subfields are statistically independent. This is not really satisfied in practice. Therefore, it only gives rough estimations (cf. Lacasa & Kunz 2017; Jiang et al. 2023). Since we mainly focus on comparisons of the two schemes for measuring MFs, this issue, in principle, does not affect our conclusions. To solve this issue, one can use a large number of simulation realizations to give accurate but expensive covariance estimates. We leave this for future works.

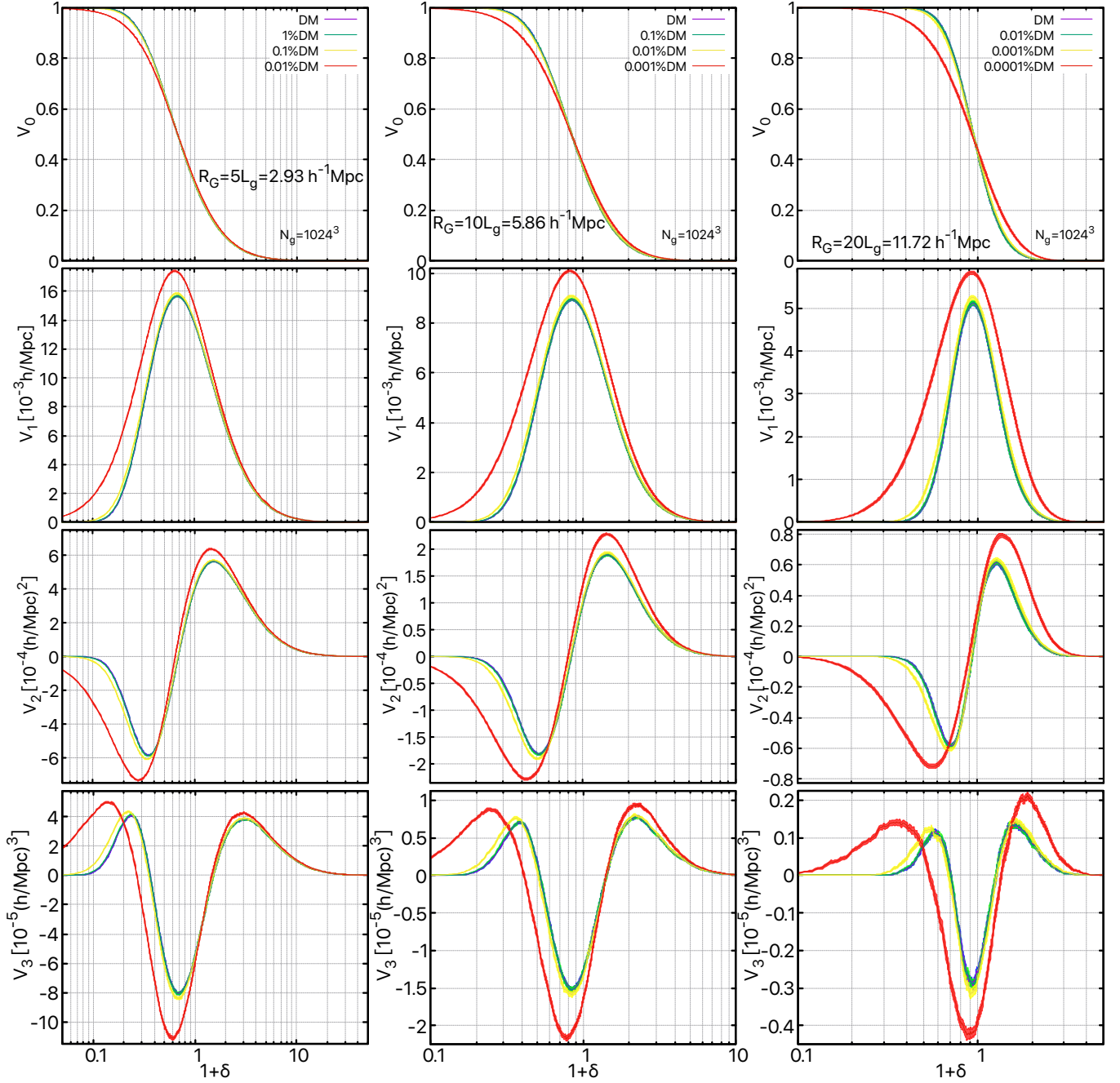


Figure 12. The MFs of noise-free field and various downgraded fields under different smoothing lengths. Left panels: MFs of noise-free field (blue lines) and 1% (green lines), 0.1% (yellow lines), 0.01% (red lines) downgraded fields, under $R_G = 5L_g = 2.93 h^{-1} \text{Mpc}$. Middle panels: MFs of noise-free field (blue lines) and 0.1% (green lines), 0.01% (yellow lines), 0.001% (red lines) downgraded fields, under $R_G = 10L_g = 5.86 h^{-1} \text{Mpc}$. Right panels: MFs of noise-free field (blue lines) and 0.01% (green lines), 0.001% (yellow lines), 0.0001% (red lines) downgraded fields, under $R_G = 20L_g = 11.72 h^{-1} \text{Mpc}$. Here, $L_g = L/N_g^{1/3} \approx 0.59 h^{-1} \text{Mpc}$ is the grid cell size. Shaded bands show 1- σ scatterers. As shown, the MFs of %1, %0.1, %0.01 downgraded fields under smoothing lengths of $R_G = 2.93 h^{-1} \text{Mpc}$, $R_G = 5.86 h^{-1} \text{Mpc}$, $R_G = 11.72 h^{-1} \text{Mpc}$ overlap with the MFs of noise-free field under the corresponding smoothing lengths, respectively, within 1- σ accuracy range. That is, in each panel, the green line basically overlaps with the blue line. This means that under these smoothing lengths, the shot noise effects on MFs of corresponding downgraded fields can be sufficiently smoothed out. As downgrading level increases, these smoothing lengths are inadequate to eliminate shot noise effects on MFs. Consequently, in each panel, the yellow and red lines deviate from the blue line, illustrating how shot noises affect the measurements of CIC+GS MFs.

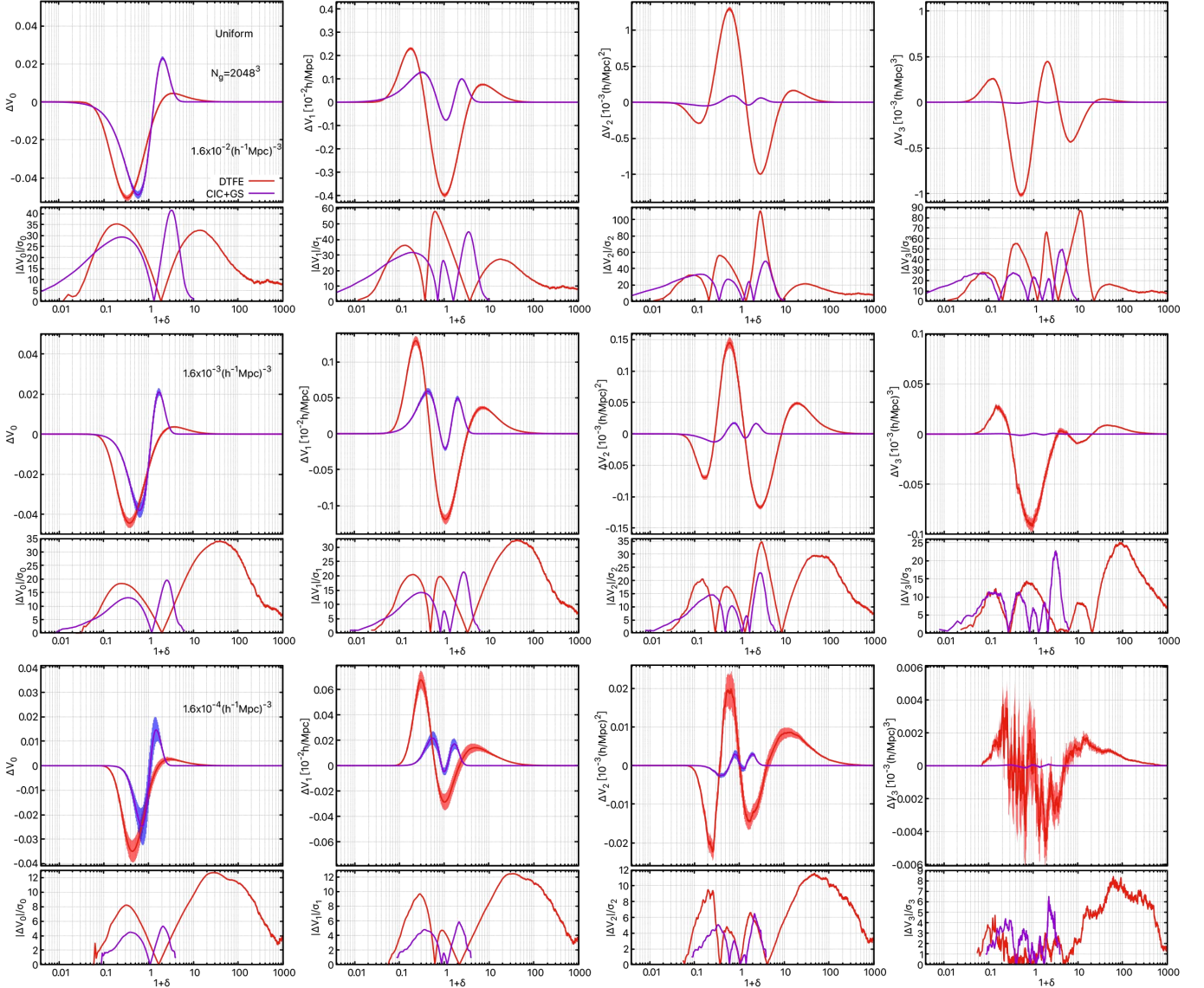


Figure 13. The RSD signals and corresponding S/N ratios in MFs. The RSD signals are obtained by measuring the differences between MFs of uniform-weighted halo fields in redshift space and real space (i.e., ΔV_i ; cf. Equation (18)). The S/N ratios are calculated through $|\Delta V_i|/\sigma_i$, where σ_i is the $1-\sigma$ error on ΔV_i . From left to right columns, the results for V_0 , V_1 , V_2 , and V_3 are presented, respectively. From top to bottom, each row corresponds to the case of halo number density of $1.6 \times 10^{-2} (h^{-1} \text{Mpc})^{-3}$, $1.6 \times 10^{-3} (h^{-1} \text{Mpc})^{-3}$, and $1.6 \times 10^{-4} (h^{-1} \text{Mpc})^{-3}$, respectively. For each panel, top subplot shows RSD signals and bottom subplot presents RSD S/N ratios, where blue and red curves are for CIC+GS and DTFE cases, respectively. In CIC+GS case, for halo number densities in descending order, the smoothing lengths $R_G = 6.8 h^{-1} \text{Mpc}$, $R_G = 14.6 h^{-1} \text{Mpc}$, and $R_G = 31.4 h^{-1} \text{Mpc}$ are adopted, respectively. These smoothing lengths are determined by the mean halo spacings of our halo samples. Shaded band shows $1-\sigma$ scatter.

$[v_{\text{lower}}, v_{\text{upper}}], n_{d_{32}}, n_{d_{64}}$	$\bar{n}_h = 1.6 \times 10^{-2} (h^{-1} \text{Mpc})^{-3}$	$\bar{n}_h = 1.6 \times 10^{-3} (h^{-1} \text{Mpc})^{-3}$	$\bar{n}_h = 1.6 \times 10^{-4} (h^{-1} \text{Mpc})^{-3}$
CIC+GS MFs	[0.012, 6.907], 17, 36	[0.048, 4.605], 12, 25	[0.168, 3.028], 8, 15
DTFE MFs	[0.032, 1000], 26, 56	[0.048, 1000], 25, 52	[0.072, 1000], 24, 48

Table 1. The density threshold ranges and numbers of data points used in our Fisher forecasts. For both CIC+GS and DTFE MFs, we show these values in various halo number density cases. Here, $n_{d_{32}}$ and $n_{d_{64}}$ indicate the numbers of remaining data points derived from the original $n_b = 32$ and $n_b = 64$ data points, respectively. In lower halo number density cases, the induced larger smoothing effects make the density fields more uniform. As a consequence, the MFs are squeezed towards intermediate density thresholds (cf. Section 6.2). Therefore, the actually used density threshold ranges become narrower, and the corresponding numbers of remaining data points decrease (cf. Fig. 14).

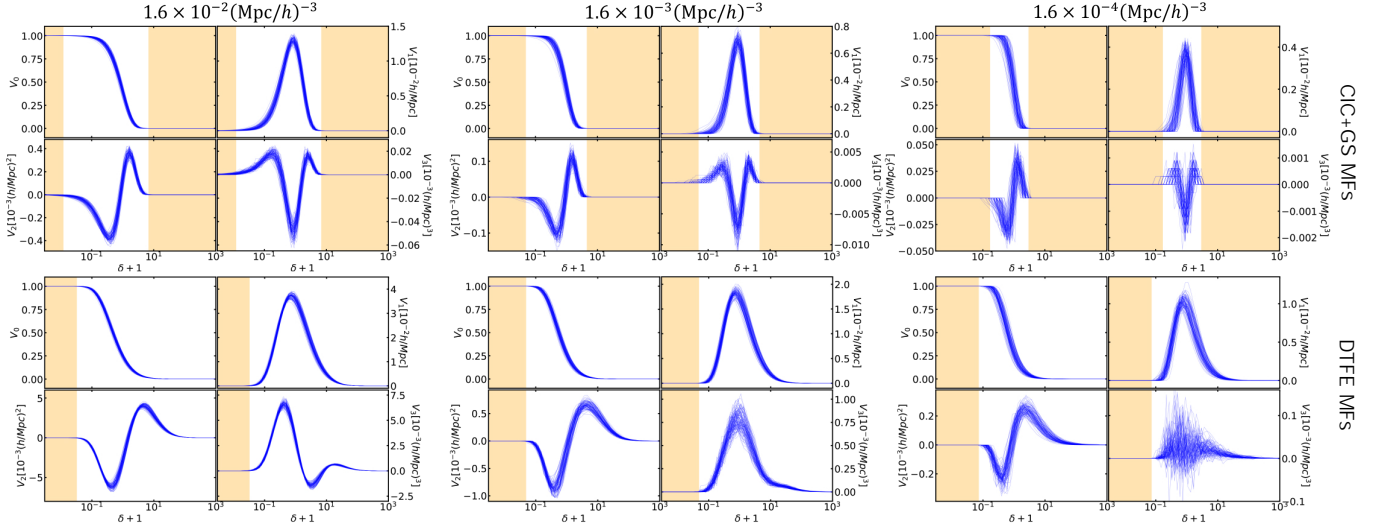


Figure 14. The MFs of subfields. The upper panels are for CIC+MFs, and the lower panels are for DTFE MFs. From left to right, each panel shows the case of halo number density of $1.6 \times 10^{-2} (h^{-1}\text{Mpc})^{-3}$, $1.6 \times 10^{-3} (h^{-1}\text{Mpc})^{-3}$, and $1.6 \times 10^{-4} (h^{-1}\text{Mpc})^{-3}$, respectively. For each panel, we show 100 sets of MFs, which are randomly selected from the MFs of 512 subfields. Here, each V_i has $n_b = 64$ data points, and the unshielded regions indicate the density threshold ranges actually used in our calculations for Fisher forecasts (cf. Table 1).

point, we get

$$\frac{\partial \mu}{\partial \theta} \simeq \frac{\mu(\theta + d\theta) - \mu(\theta - d\theta)}{2d\theta} = \frac{\Delta V_i^{(z)}(v)}{\Delta(f\sigma_8)}. \quad (\text{C5})$$

In our calculation, we select n_b data points for each $V_i(v)$. These data points are evenly distributed within $[v_{\min}, v_{\max}]$ in logarithmic coordinate. To avoid any problems sourced from the irreversibility of covariance matrices, the used density threshold range $[v_{\text{lower}}, v_{\text{upper}}]$ should be narrowed as halo number density decreases. This will result in a decrease in the number of data points actually used in calculations. We illustrate this in Fig. 14¹⁵ (cf. the unshielded regions) and Table 1. In order to draw conclusions as reliable as possible, two n_b cases are tested, namely $n_b = 32$ (cf. Fig. 11) and $n_b = 64$ (cf. Fig. 15). This provides a consistency check for

our methodology. In general, in comparison with Fig. 11, the predictive errors in Fig. 15 are relatively smaller, depending on different cases. Specifically, as the number of data points increases, we find the followings:

- For CIC+GS MFs, the predictive errors exhibit minimal changes, except for a few cases, e.g., the case of V_0 with $n_h = 1.6 \times 10^{-2} (h^{-1}\text{Mpc})^{-3}$;
- For DTFE MFs, the predictive errors remain relatively stable in the case of $n_h = 1.6 \times 10^{-2} (h^{-1}\text{Mpc})^{-3}$, but show a noticeable decrease in the cases of $n_h = 1.6 \times 10^{-3} (h^{-1}\text{Mpc})^{-3}$ and $n_h = 1.6 \times 10^{-4} (h^{-1}\text{Mpc})^{-3}$.

Nevertheless, the performance of DTFE MFs still significantly outperforms that of CIC+GS MFs, thus our conclusions do not change.

REFERENCES

- Abel, T., Hahn, O., & Kaehler, R. 2012, *MNRAS*, **427**, 61
 Alam, S., Ata, M., Bailey, S., et al. 2017, *MNRAS*, **470**, 2617
 Appleby, S., Chingangbam, P., Park, C., et al. 2018a, *ApJ*, **858**, 87
 Appleby, S., Chingangbam, P., Park, C., Yogendran, K. P., & Joby, P. K. 2018b, *ApJ*, **863**, 200
 Appleby, S., Park, C., Hong, S. E., Hwang, H. S., & Kim, J. 2020, *ApJ*, **896**, 145
 Appleby, S., Park, C., Hong, S. E., et al. 2021, *ApJ*, **907**, 75
 Appleby, S., Park, C., Hong, S. E., & Kim, J. 2017, *ApJ*, **836**, 45
 Appleby, S., Park, C., Hong, S. E., & Kim, J. 2018c, *ApJ*, **853**, 17
 Appleby, S., Park, C., Pranav, P., et al. 2022, *ApJ*, **928**, 108
 Aragon-Calvo, M. A. 2021, *MNRAS*, **503**, 557
 Aragon-Calvo, M. A., Jones, B. J. T., van de Weygaert, R., & van der Hulst, J. M. 2007, *A&A*, **474**, 315
 Aragon-Calvo, M. A., Platen, E., van de Weygaert, R., & Szalay, A. S. 2010, *ApJ*, **723**, 364
 Aragon-Calvo, M. A., Shandarin, S. F., & Szalay, A. 2010, arXiv e-prints, arXiv:1006.4178
 Arnalte-Mur, P., Labatie, A., Clerc, N., et al. 2012, *A&A*, **542**, A34
 Barrow, J. D., Bhavsar, S. P., & Sonoda, D. H. 1985, *MNRAS*, **216**, 17
 Basilakos, S. 2003, *MNRAS*, **344**, 602
 Bautista, J. E., Paviot, R., Vargas Magaña, M., et al. 2021, *MNRAS*, **500**, 736
 Bermejo, R., Wilding, G., van de Weygaert, R., et al. 2024, *MNRAS*, **529**, 4325
 Bernardeau, F., & van de Weygaert, R. 1996, *MNRAS*, **279**, 693
 Blake, C., James, J. B., & Poole, G. B. 2014, *MNRAS*, **437**, 2488
 Cai, Y.-C., Bernstein, G., & Sheth, R. K. 2011, *MNRAS*, **412**, 995
 Cautun, M., van de Weygaert, R., & Jones, B. J. T. 2013, *MNRAS*, **429**, 1286
 Cautun, M. C., & van de Weygaert, R. 2011a, arXiv e-prints, arXiv:1105.0370
 Cautun, M. C., & van de Weygaert, R. 2011b, The DTFE public software: The Delaunay Tessellation Field Estimator code
 Chan, K. C., Hamaus, N., & Desjacques, V. 2014, *PhRvD*, **90**, 103521
 Chen, J., Zhang, P., Zheng, Y., Yu, Y., & Jing, Y. 2018, *ApJ*, **861**, 58
 Cheng, S., & Ménard, B. 2021, *MNRAS*, **507**, 1012

¹⁵ We only display the results of $n_b = 64$, considering the striking similarity between these results and those of $n_b = 32$.

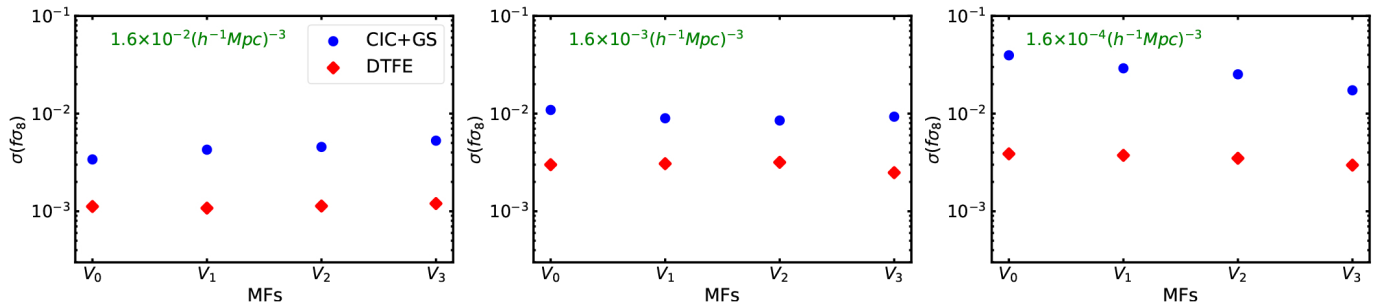


Figure 15. The same as Fig. 11, but for the case of $n_b = 64$.

- Cheng, S., Ting, Y.-S., Ménard, B., & Bruna, J. 2020, *MNRAS*, **499**, 5902
- Choi, Y.-Y., Park, C., Kim, J., et al. 2010, *ApJS*, **190**, 181
- Codis, S., Pichon, C., Pogosyan, D., Bernardeau, F., & Matsubara, T. 2013, *MNRAS*, **435**, 531
- de Jong, R. S., Bellido-Tirado, O., Chiappini, C., et al. 2012, in *Society of Photo-Optical Instrumentation Engineers (SPIE) Conference Series*, Vol. 8446, *Ground-based and Airborne Instrumentation for Astronomy IV*, ed. I. S. McLean, S. K. Ramsay, & H. Takami, 84460T
- de Lapparent, V., Geller, M. J., & Huchra, J. P. 1991, *ApJ*, **369**, 273
- DESI Collaboration, Aghamousa, A., Aguilar, J., et al. 2016, arXiv e-prints, arXiv:1611.00036
- Doré, O., Bock, J., Ashby, M., et al. 2014, arXiv e-prints, arXiv:1412.4872
- Doré, O., Hirata, C., Wang, Y., et al. 2018, arXiv e-prints, arXiv:1804.03628
- Dougllass, K., Veyrat, D., O'Neill, S., et al. 2022, *The Journal of Open Source Software*, **7**, 4033
- Dougllass, K. A., Veyrat, D., & BenZvi, S. 2023, *ApJS*, **265**, 7
- Ducout, A., Bouchet, F. R., Colombi, S., Pogosyan, D., & Prunet, S. 2013, *MNRAS*, **429**, 2104
- Eisenstein, D. J., Zehavi, I., Hogg, D. W., et al. 2005, *ApJ*, **633**, 560
- Elbers, W., & van de Weygaert, R. 2019, *MNRAS*, **486**, 1523
- Elbers, W., & van de Weygaert, R. 2023, *MNRAS*, **520**, 2709
- Ellis, R., & Dawson, K. 2019, in *Bulletin of the American Astronomical Society*, Vol. 51, 45
- Emberson, J. D., Yu, H.-R., Inman, D., et al. 2017, *Research in Astronomy and Astrophysics*, **17**, 085
- Euclid Collaboration, Blanchard, A., Camera, S., et al. 2020, *A&A*, **642**, A191
- Fang, F., Forero-Romero, J., Rossi, G., Li, X.-D., & Feng, L.-L. 2019, *MNRAS*, **485**, 5276
- Fang, W., Li, B., & Zhao, G.-B. 2017, *PhRvL*, **118**, 181301
- Feldbrugge, J. 2024, arXiv e-prints, arXiv:2402.16234
- Gay, C., Pichon, C., & Pogosyan, D. 2012, *PhRvD*, **85**, 023011
- Giri, S. K., & Mellema, G. 2021, *MNRAS*, **505**, 1863
- Gong, Y., Liu, X., Cao, Y., et al. 2019, *ApJ*, **883**, 203
- Gott, J. Richard, I., Melott, A. L., & Dickinson, M. 1986, *ApJ*, **306**, 341
- Gott, J. Richard, I., Weinberg, D. H., & Melott, A. L. 1987, *ApJ*, **319**, 1
- Gott, J. Richard, I., Miller, J., Thuan, T. X., et al. 1989, *ApJ*, **340**, 625
- Haas, M. R., Schaye, J., & Jeason-Daniel, A. 2012, *MNRAS*, **419**, 2133
- Hadwiger, H. Springer, Berlin, 1957, *Vorlesungen über Inhalt, Oberfläche und Isoperimetrie*
- Hamaus, N., Seljak, U., & Desjacques, V. 2011, *PhRvD*, **84**, 083509
- Hamaus, N., Seljak, U., & Desjacques, V. 2012, *PhRvD*, **86**, 103513
- Hamaus, N., Seljak, U., Desjacques, V., Smith, R. E., & Baldauf, T. 2010, *PhRvD*, **82**, 043515
- Hamilton, A. J. S. 2001, *MNRAS*, **322**, 419
- Hamilton, A. J. S., Gott, J. Richard, I., & Weinberg, D. 1986, *ApJ*, **309**, 1
- Harnois-Déraps, J., Pen, U.-L., Iliev, I. T., et al. 2013, *MNRAS*, **436**, 540
- Hartlap, J., Simon, P., & Schneider, P. 2007, *A&A*, **464**, 399
- Hikage, C., Coles, P., Grossi, M., et al. 2008, *MNRAS*, **385**, 1613
- Hikage, C., Komatsu, E., & Matsubara, T. 2006, *ApJ*, **653**, 11
- Hikage, C., Schmalzing, J., Buchert, T., et al. 2003, *PASJ*, **55**, 911
- Hill, G. J., Gebhardt, K., Komatsu, E., et al. 2008, in *Astronomical Society of the Pacific Conference Series*, Vol. 399, *Panoramic Views of Galaxy Formation and Evolution*, ed. T. Kodama, T. Yamada, & K. Aoki, 115
- Hou, J., Cahn, R. N., Philcox, O. H. E., & Slepian, Z. 2021, arXiv e-prints, arXiv:2108.01714
- Jackson, J. C. 1972, *MNRAS*, **156**, 1P
- Jalali Kanafi, M. H., Ansarifard, S., & Movahed, S. M. S. 2023, arXiv e-prints, arXiv:2311.13520
- James, J. B. 2012, *ApJ*, **751**, 40
- Jamieson, D., & Loverde, M. 2021, *PhRvD*, **103**, 103522
- Jiang, A., Liu, W., Fang, W., & Zhao, W. 2021, arXiv e-prints, arXiv:2108.03851
- Jiang, A., Liu, W., Li, B., et al. 2023, arXiv e-prints, arXiv:2305.04520
- Jing, Y. 2019, *Science China Physics, Mechanics, and Astronomy*, **62**, 19511
- Jing, Y. P., & Suto, Y. 2002, *ApJ*, **574**, 538
- Jing, Y. P., Suto, Y., & Mo, H. J. 2007, *ApJ*, **657**, 664
- Jost, J., & Jost, J. 2008, *Riemannian geometry and geometric analysis*, Vol. 42005 (Springer)
- Kaiser, N. 1987, *MNRAS*, **227**, 1
- Kim, Y.-R., Choi, Y.-Y., Kim, S. S., et al. 2014, *ApJS*, **212**, 22
- Kreisch, C. D., Pisani, A., Carbone, C., et al. 2019, *MNRAS*, **488**, 4413
- Lacasa, F., & Kunz, M. 2017, *A&A*, **604**, A104
- Lahav, O., Lilje, P. B., Primack, J. R., & Rees, M. J. 1991, *MNRAS*, **251**, 128
- Laureijs, R., Amiaux, J., Arduini, S., et al. 2011, arXiv e-prints, arXiv:1110.3193
- Lippich, M., & Sánchez, A. G. 2021, *MNRAS*, **508**, 3771
- Liu, J., Petri, A., Haiman, Z., et al. 2015a, *PhRvD*, **91**, 063507
- Liu, W., Jiang, A., & Fang, W. 2022, arXiv e-prints, arXiv:2204.02945
- Liu, X., Pan, C., Li, R., et al. 2015b, *MNRAS*, **450**, 2888
- Liu, Y., Yu, Y., & Li, B. 2021, *ApJS*, **254**, 4
- Liu, Y., Yu, Y., Yu, H.-R., & Zhang, P. 2020, *PhRvD*, **101**, 063515
- LSST Science Collaboration, Abell, P. A., Allison, J., et al. 2009, arXiv e-prints, arXiv:0912.0201
- Marques, G. A., Liu, J., Zorrilla Matilla, J. M., et al. 2019, *JCAP*, **2019**, 019
- Martínez, V. J., Paredes, S., & Saar, E. 1993, *MNRAS*, **260**, 365
- Martínez, V. J., Starck, J.-L., Saar, E., et al. 2005, *ApJ*, **634**, 744
- Matsubara, T. 1994, *ApJL*, **434**, L43
- Matsubara, T. 1996, *ApJ*, **457**, 13
- Matsubara, T. 2003, *ApJ*, **584**, 1
- Matsubara, T. 2010, *PhRvD*, **81**, 083505
- Matsubara, T., Hikage, C., & Kuriki, S. 2022, *PhRvD*, **105**, 023527
- Matsubara, T., & Kuriki, S. 2021, *PhRvD*, **104**, 103522
- Matsubara, T., & Suto, Y. 1996, *ApJ*, **460**, 51
- Mecke, J. 1979, *ZAMM - Journal of Applied Mathematics and Mechanics / Zeitschrift für Angewandte Mathematik und Mechanik*, **59**, 286
- Mecke, K. R., Buchert, T., & Wagner, H. 1994, *A&A*, **288**, 697
- Melott, A. L., Cohen, A. P., Hamilton, A. J. S., Gott, J. Richard, I., & Weinberg, D. H. 1989, *ApJ*, **345**, 618
- Melott, A. L., & Dominik, K. G. 1993, *ApJS*, **86**, 1

- Melott, A. L., Weinberg, D. H., & Gott, J. Richard, I. 1988, *ApJ*, **328**, 50
- Milnor, J. W. 1963, Morse theory No. 51 (Princeton university press)
- Moon, J., Valcin, D., Rashkovetskiy, M., et al. 2023, *MNRAS*, **525**, 5406
- Morse, M. 1934, The calculus of variations in the large, Vol. 18 (American Mathematical Soc.)
- Nadathur, S., Carter, P. M., Percival, W. J., Winther, H. A., & Bautista, J. E. 2019, *PhRvD*, **100**, 023504
- Naidoo, K., Massara, E., & Lahav, O. 2021, arXiv e-prints, arXiv:2111.12088
- Neyrinck, M. C. 2008, *MNRAS*, **386**, 2101
- Novikov, D., Colombi, S., & Doré, O. 2006, *MNRAS*, **366**, 1201
- Paranjape, A., & Alam, S. 2020, *MNRAS*, **495**, 3233
- Parihar, P., Vogeley, M. S., Gott, J. Richard, I., et al. 2014, *ApJ*, **796**, 86
- Park, C., & Gott, J. R., I. 1991, *ApJ*, **378**, 457
- Park, C., Kim, J., & Gott, J. Richard, I. 2005, *ApJ*, **633**, 1
- Park, C., & Kim, Y.-R. 2010, *ApJL*, **715**, L185
- Percival, W. J., Yèche, C., Bilicki, M., et al. 2019, arXiv e-prints, arXiv:1903.03158
- Petri, A., Liu, J., Haiman, Z., et al. 2015, *PhRvD*, **91**, 103511
- Philcox, O. H. E., & Slepian, Z. 2021, arXiv e-prints, arXiv:2106.10278
- Philcox, O. H. E., Slepian, Z., Hou, J., et al. 2022, *MNRAS*, **509**, 2457
- Planck Collaboration, Ade, P. A. R., Aghanim, N., et al. 2016, *A&A*, **594**, A17
- Platen, E., van de Weygaert, R., & Jones, B. J. T. 2007, *MNRAS*, **380**, 551
- Pogosyan, D., Gay, C., & Pichon, C. 2009, *PhRvD*, **80**, 081301
- Pranav, P., Edelsbrunner, H., van de Weygaert, R., et al. 2017, *MNRAS*, **465**, 4281
- Pranav, P., van de Weygaert, R., Vegter, G., et al. 2019, *MNRAS*, **485**, 4167
- Repp, A., & Szapudi, I. 2020, *MNRAS*, **498**, L125
- Romano-Díaz, E., & van de Weygaert, R. 2007, *MNRAS*, **382**, 2
- Sahni, V., Sathyaprakash, B. S., & Shandarin, S. F. 1998, *ApJL*, **495**, L5
- Schaap, W. E. 2007, PhD thesis, University of Groningen, Netherlands
- Schaap, W. E., & van de Weygaert, R. 2000, *A&A*, **363**, L29
- Schlegel, D., Kollmeier, J. A., & Ferraro, S. 2019, in *Bulletin of the American Astronomical Society*, Vol. 51, 229
- Schmalzing, J., & Buchert, T. 1997, *ApJL*, **482**, L1
- Schneider, R. 1993, Convex Bodies: The Brunn-Minkowski Theory, Encyclopedia of Mathematics and its Applications (Cambridge University Press)
- Seljak, U., Hamaus, N., & Desjacques, V. 2009, *PhRvL*, **103**, 091303
- Shan, H. Y., Kneib, J.-P., Comparat, J., et al. 2014, *MNRAS*, **442**, 2534
- Shandarin, S., Habib, S., & Heitmann, K. 2012, *PhRvD*, **85**, 083005
- Sheth, J. V., Sahni, V., Shandarin, S. F., & Sathyaprakash, B. S. 2003, *MNRAS*, **343**, 22
- Sousbie, T. 2011, *MNRAS*, **414**, 350
- Sousbie, T., Pichon, C., Colombi, S., Novikov, D., & Pogosyan, D. 2008, *MNRAS*, **383**, 1655
- Sousbie, T., Pichon, C., & Kawahara, H. 2011, *MNRAS*, **414**, 384
- Suárez-Pérez, J. F., Camargo, Y., Li, X.-D., & Forero-Romero, J. E. 2021, *ApJ*, **922**, 204
- Sutter, P. M., Lavaux, G., Hamaus, N., et al. 2015, *Astronomy and Computing*, **9**, 1
- Takada, M., Ellis, R. S., Chiba, M., et al. 2014, *PASJ*, **66**, R1
- Tomita, H. 1990, STATISTICS AND GEOMETRY OF RANDOM INTERFACE SYSTEMS, 113
- Uhlemann, C., Friedrich, O., Villaescusa-Navarro, F., Banerjee, A., & Codis, S. 2020, *MNRAS*, **495**, 4006
- van de Weygaert, R., Aragon-Calvo, M. A., Jones, B. J. T., & Platen, E. 2009, arXiv e-prints, arXiv:0912.3448
- van de Weygaert, R., & Schaap, W. 2009, in *Data Analysis in Cosmology*, ed. V. J. Martínez, E. Saar, E. Martínez-González, & M. J. Pons-Bordería, Vol. 665, 291
- van de Weygaert, R., Vegter, G., Edelsbrunner, H., et al. 2011, in *Lecture Notes in Computer Science*, Vol. 6970, 60
- Wang, X., Chen, X., & Park, C. 2012, *ApJ*, **747**, 48
- Wiegand, A., Buchert, T., & Ostermann, M. 2014, *MNRAS*, **443**, 241
- Wilding, G., Nevenzeel, K., van de Weygaert, R., et al. 2021, *MNRAS*, **507**, 2968
- Yip, J. H. T., Biagetti, M., Cole, A., Viswanathan, K., & Shiu, G. 2024, arXiv e-prints, arXiv:2403.13985
- Yu, H.-R., Emberson, J. D., Inman, D., et al. 2017, *Nature Astronomy*, **1**, 0143
- Zhang, Y., Springel, V., & Yang, X. 2010, *ApJ*, **722**, 812
- Zhao, C., Kitaura, F.-S., Chuang, C.-H., et al. 2015, *MNRAS*, **451**, 4266
- Zhao, C., Tao, C., Liang, Y., Kitaura, F.-S., & Chuang, C.-H. 2016, *MNRAS*, **459**, 2670
- Zunckel, C., Gott, J. R., & Lunnan, R. 2011, *MNRAS*, **412**, 1401